Computers & Fluids 116 (2015) 129–147

Contents lists available at ScienceDirect

Computers & Fluids

journal homepage: www.elsevier.com/locate/compfluid

Direct numerical simulation of turbulent flow over a rough surface based on a surface scan

Angela Busse [a,*], Mark Lützner [b], Neil D. Sandham [c]

[a] School of Engineering, University of Glasgow, Glasgow G12 8QQ, United Kingdom
[b] Universität Stuttgart, Stuttgart, Germany
[c] Faculty of Engineering and the Environment, University of Southampton, Southampton SO17 1BJ, United Kingdom

ARTICLE INFO

Article history:
Received 3 September 2014
Received in revised form 29 January 2015
Accepted 6 April 2015
Available online 11 April 2015

Keywords:
Rough-wall turbulent channel flow
Direct numerical simulation
Surface topography

ABSTRACT

Typical engineering rough surfaces show only limited resemblance to the artificially constructed rough surfaces that have been the basis of most previous fundamental research on turbulent flow over rough walls. In this article flow past an irregular rough surface is investigated, based on a scan of a rough graphite surface that serves as a typical example for an irregular rough surface found in engineering applications. The scanned map of surface height versus lateral coordinates is filtered in Fourier space to remove features on very small scales and to create a smoothly varying periodic representation of the surface. The surface is used as a no-slip boundary in direct numerical simulations of turbulent channel flow. For the resolution of the irregular boundary an iterative embedded boundary method is employed. The effects of the surface filtering on the turbulent flow are investigated by studying a series of surfaces with decreasing level of filtering. Mean flow, Reynolds stress and dispersive stress profiles show good agreement once a sufficiently large number of Fourier modes are retained. However, significant differences are observed if only the largest surface features are resolved. Strongly filtered surfaces give rise to a higher mean-flow velocity and to a higher variation of the streamwise velocity in the roughness layer compared with weakly filtered surfaces. In contrast, for the weakly filtered surfaces the mean flow is reversed over most of the lower part of the roughness sublayer and higher levels of dispersive shear stress are found.

1. Introduction

Rough surfaces affect the flow in many engineering systems, since many processes can cause surface roughness. Roughness can be a side-effect of the production of a surface, where a higher level of finishing would be uneconomical (see [29]), or can develop over time due to erosion or the accumulation of deposits. In turbomachinery applications several different processes, such as the deposition of fuel and airborne contaminants, pitting, erosion and corrosion, can all contribute to the generation of roughness on turbine blades and vanes during service (see [8]). In the case of ships, both organic and inorganic fouling processes lead to the growth of roughness on the hull resulting in increased fuel consumption (see [59,57,24]). The growth of surface roughness is one of the processes of decay and, as such, is inevitable in the long term for most engineering components. On a geophysical scale, many examples of rough surfaces can be found which affect atmospheric flows (see [2]). For example, plant canopies (see [17]) and urban roughness (see [12,14]) can influence the regional climate.

Rough surfaces can be classified as regular or irregular/random. Most regular rough surfaces are built from simple geometric patterns which possess one or a small number of characteristic length scales. They are usually the product of a deliberate surface design, which is intended to improve specific properties of the engineering system in which they occur. For example, drag reduction can be achieved using riblet surfaces, which are formed of streamwise aligned, regularly spaced grooves (see [4]). The efficiency of heat exchangers can be improved using surface dimples (see [34]), which are often arranged in a hexagonal pattern.

However, most engineering rough surfaces are irregular due to the nature of the processes by which they are created. Even surface finishing processes, such as grinding or boring, which might be expected to generate regular rough surfaces, in fact produce irregular surfaces (see [55]). On atmospheric-relevant scales most roughness is irregular. Exceptions can again be attributed to deliberate human design, such as city planning leading to regular urban

* Corresponding author. Tel.: +44 (0)141 330 4321.
E-mail address: angela.busse@glasgow.ac.uk (A. Busse).

http://dx.doi.org/10.1016/j.compfluid.2015.04.008
0045-7930/

roughness in the form of regularly spaced blocks of houses (see [26]).

Despite the fact that most rough surfaces are irregular, most previous fundamental research on turbulent flow over rough surfaces has concentrated on highly regular roughness geometries. The rough surfaces used in the experiments of Schlichting [48], where roughness elements in the form of spheres, hemispherical caps and cones were arranged in uniform patterns, are a typical example. Surfaces composed from blocks and bars (see e.g. [32,31,30,27]) are another very common roughness configuration. These rough surfaces have proven popular, since they are easy to build for wind tunnel experiments. They also possess a simple geometry that is comparatively easy to represent in direct numerical simulation codes. A further advantage of simple regular rough surfaces is that they possess a clearly defined roughness height and are easy to reproduce. However, their limited resemblance to irregular rough surfaces makes their use as a general roughness model problematic. Highly regular rough surfaces can exhibit behaviour not commonly found for irregular rough surfaces. For example, a regular arrangement of roughness elements can lead to strong shielding effects (see [13]). The riblet effect (see [4]) is probably the most extreme example of atypical roughness behaviour introduced by highly regular roughness. Therefore, the study of flow over irregular roughness cannot be replaced by studies of flow over highly regular rough surfaces.

A number of experimental studies have investigated flow over irregular roughness; the best known example being the study of Nikuradse [42] on turbulent flow over rough surfaces made from sieved sand grains. This approach was adopted by others, e.g. rough surfaces made up from sand and round pebbles have been used in flow channel experiments (see [18]), while packed gravel chips (see [11]), abrasive sheets (see [46,5]) and scratched surfaces (see [50]) have been used to produce rough surfaces for wind tunnel experiments. In most cases, these surfaces have been used as a convenient way to construct a rough surface with a reasonably well defined roughness height and not necessarily because they were of particular practical interest. With the advent of better moulding techniques and 3D printing, rough surfaces models, which are based on roughness found in technical applications, have started to be used in rough-wall turbulent flow experiments. Bons [7] used scaled models of rough surfaces based on scans of damaged turbine surfaces in wind tunnel experiments. These surfaces were later also studied by Wu and Christensen [61,62]. A systematic study of the effect of irregular roughness on turbulent channel flow using roughened steel plates was conducted by Rij et al. [58].

Only a small number of highly resolved numerical studies have been performed on turbulent flow over irregular roughness. Napoli et al. [41] studied flow over irregular wavy rough surfaces. In these simulations the roughness was uniform in the spanwise direction. In a recent study, Cardillo et al. [10] investigated the development of a turbulent boundary layer over a surface that was based on a laser scan of sandpaper.

When producing a rough surface model for a wind-tunnel experiment or a numerical simulation, some form of filtering will usually occur. Filtering is necessary to remove measurement noise which typically occurs on small spatial scales. In addition, the process for producing a model for a wind-tunnel, e.g. using 3D printing, will usually not perfectly resolve every small-scale feature. The surface may also need to be modified in order to allow the continuous tiling of a wind tunnel. In simulations, surface modification and filtering usually need to be imposed to satisfy boundary conditions and limit the computational expense.

In the experimental studies of Mejia-Alvarez and Christensen [37,38] the influence of surface filtering using singular value decomposition was studied. In this paper a different type of surface filtering, low-pass Fourier filtering, is investigated. The effect of this type of surface filtering on turbulent rough-wall channel flow is studied systematically using a range of surfaces based on a scan of a graphite surface. This study also enables the investigation of the effects of small-scale surface features on turbulent flow past an irregular rough wall. In the first part of this paper (see Section 2) we present the method used for simulating flow over a irregular surface based on a surface scan. The influence of the small scale structure of the surface on the turbulent flow is then investigated in Section 3. A short summary is given in Section 4.

2. Methodology

2.1. Flow simulation

The incompressible Navier–Stokes equations for a fluid with uniform density ρ and kinematic viscosity ν are solved for turbulent channel flow. A standard finite difference code is employed which operates on a staggered grid. Second order central differences are used for the discretisation of the spatial derivatives. The second order Adams–Bashforth scheme is used for the time integration. In the smooth-wall reference case the code has been previously validated [9].

To resolve the rough wall an embedded boundary method is employed which is a variation of the method of Yang and Balaras [64]. By introducing an extra force term $\vec{f}_{\text{emb}}$ in the Navier–Stokes equations zero velocity is enforced at the solid boundary. The solid boundary is implicitly defined as the zero-level set Γ of the signed distance function $\psi(x,y,z)$. The signed distance function $\psi(x,y,z)$ is positive in the fluid domain, negative in the solid domain and zero on the boundary. $\hat{n}_\Gamma$ is the unit normal vector pointing into the solid domain (see Fig. 1(a)). Based on the signed distance function ψ grid points are classified into three groups: All points in the solid boundary ($\psi < 0$) are solid points, points in the fluid domain ($\psi > 0$) which have no direct neighbour in the solid domain are bulk points, and points in the fluid domain with at least one direct neighbour in the solid domain are forcing points.

At the bulk points the time-integration scheme remains unchanged, i.e. $\vec{f}_{\text{emb}} = 0$; at solid points the force is chosen so that the velocity is zero. At the forcing points the velocity is set to the local linear representation of the velocity. This is defined by linear interpolation from the velocities at the three closest neighbouring grid points (P_1, P_2, P_3) in the fluid domain in the direction of $-\mathbf{n}_\Gamma$ and the projection of the forcing points onto the solid boundary P_Γ, which can easily be found from the level-set function ψ (see Fig. 1(b)). The velocity at P_Γ is set equal to the wall velocity, i.e. zero in the context of this paper.

The main difference between the current method and the method of Yang and Balaras [64] is the treatment of the special cases where at least one of the points P_1, P_2, P_3 is also a forcing point (see the example shown in Fig. 2(a)). Yang and Balaras [64] in this case changed the interpolation stencil, so that P_1, P_2, P_3 are all bulk points (see the example for a modified stencil shown in Fig. 2(b)). In the current method no change in the interpolation stencil is made. Instead the interpolation step is iterated for all forcing points until a maximum resulting change in interpolated velocity with respect to the previous iteration step is below a given threshold ϵ. Here $\epsilon = 1 \cdot 10^{-8}$ has been used. The iterative treatment simplifies the implementation of the method significantly. At the same time, the immersed boundary treatment typically uses less than 5% of the computational time, and the computational overhead introduced by the iterative treatment can be regarded as insignificant. The method has been validated using standard test cases in the context of turbulent rough wall flow. A comparison to the data of Maaß and Schumann [35] for turbulent flow in a channel with a lower wavy and flat upper wall is shown in Appendix A.

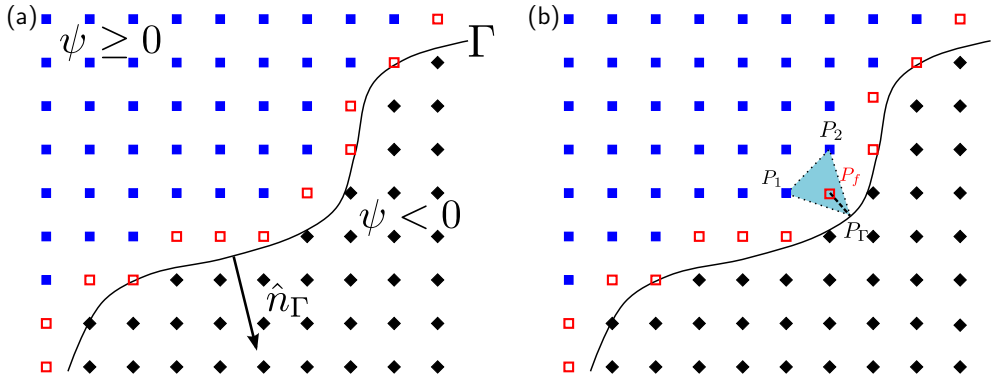

Fig. 1. (a) Classification of the grid points: bulk points (blue squares), solid points (black diamonds) and forcing points (red squares). (b) Stencil used for reconstruction of the local linear representation of velocity. A 2D example is shown for clarity. (For interpretation of the references to colour in this figure legend, the reader is referred to the web version of this article.)

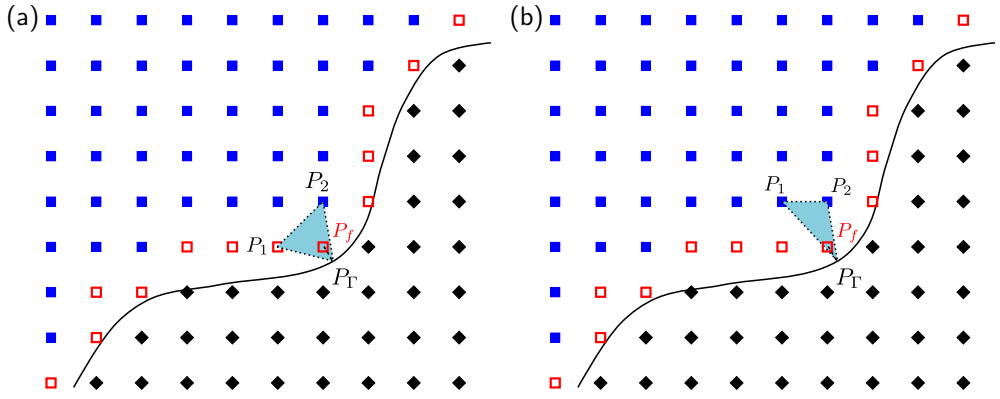

Fig. 2. (a) Example for an ambiguous stencil where P_1 is also a forcing point; (b) Yang & Balaras would modify the stencil to ensure that P_1 is not a forcing point. Symbols as in Fig. 1.

In the following simulations of rough-wall channel flow both the lower and upper wall of the channel are rough. In the streamwise (x-) and spanwise (y-) direction periodic boundary conditions are applied. The same surface pattern is used on the lower and upper surfaces. The mean channel half-height is given by δ and the mean-wall location is set to zero. The pattern on the upper surface is shifted with respect to the pattern on the lower surface. The shift applied corresponds to half of the longest wavelengths present in the surface pattern in the x- and y-direction, i.e. the pattern on the upper surface is shifted by $(\lambda_x^{\max}/2, \lambda_y^{\max}/2)$ relative to the roughness pattern on the lower surface. In most cases studied the longest wavelength corresponds to the domain size in the corresponding direction. The exception is the larger domain used for studying the domain size dependence of the results in Section 2.4, where the surface pattern is repeated.

The computational grid is uniformly spaced in the streamwise (x-) and spanwise (y-) directions. In the wall-normal (z-) direction the grid is stretched. In the region where the embedded boundary method is applied to resolve the rough surface the grid has a uniform small spacing in the z-direction (see Fig. 3). Above this layer the grid is gradually stretched towards the centre of the channel. The grid-dependence of the results is discussed in Section 2.3. In all cases the channel flow is driven by a constant mean streamwise pressure gradient $-\Pi$, which also fixes the value of the friction velocity $u_\tau = (\Pi\delta/\rho)^{1/2}$. In the following, all velocities shown are normalised with the friction velocity.

2.2. Surface data processing

Many methods exist for acquiring surface data, e.g. contact measurements with a stylus instrument (see [52]) and non-invasive optical measurements, such as focus variation microscopes or laser profilometers (see [53]). The most suitable surface measurement method depends on the material of the sample and the typical size of the roughness features. A wide range of parameters are used for the characterisation of rough surfaces. The parameters used within the context of this paper are defined in Appendix B.

Once a three-dimensional discrete map of the surface height $h_{\text{raw}}(x, y)$ has been obtained, the surface data needs to be filtered before it can be used as a rough-wall boundary condition. The raw data of the surface scan is shown in Fig. 4(a). The surface height is known on a uniform Cartesian grid, i.e. $x = 0, \Delta s, 2\Delta s, \ldots, (M-1)\Delta s$ and $y = 0, \Delta s, 2\Delta s, \ldots, (N-1)\Delta s$, where x is the streamwise, y the spanwise coordinate and Δs the spacing of the measurement points. The mean reference plane has been subtracted from the data, i.e. the mean height and slope of the surface are zero.

Before the surface height map can be used as a boundary condition for direct numerical simulations the surface data needs to be processed. This is due to the following problems: Firstly, surface scans usually contain a finite amount of measurement noise. Most of the measurement noise occurs typically on small spatial scales (see [51]) and needs to be removed. Secondly, for

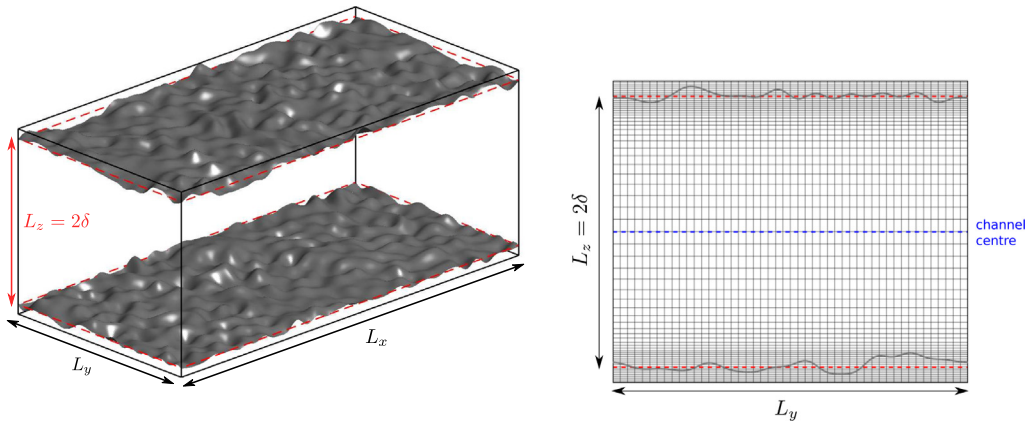

Fig. 3. Left: Illustration of the computational domain; grey: rough boundaries, black lines: edges of the computational box, dashed red lines: mean lower and upper wall location. Right: cross section in y–z plane illustrating the computational grid. Note that the computational grid shown is for illustrative purposes only. The actual grids used for the direct numerical simulations have a much finer grid spacing. (For interpretation of the references to colour in this figure legend, the reader is referred to the web version of this article.)

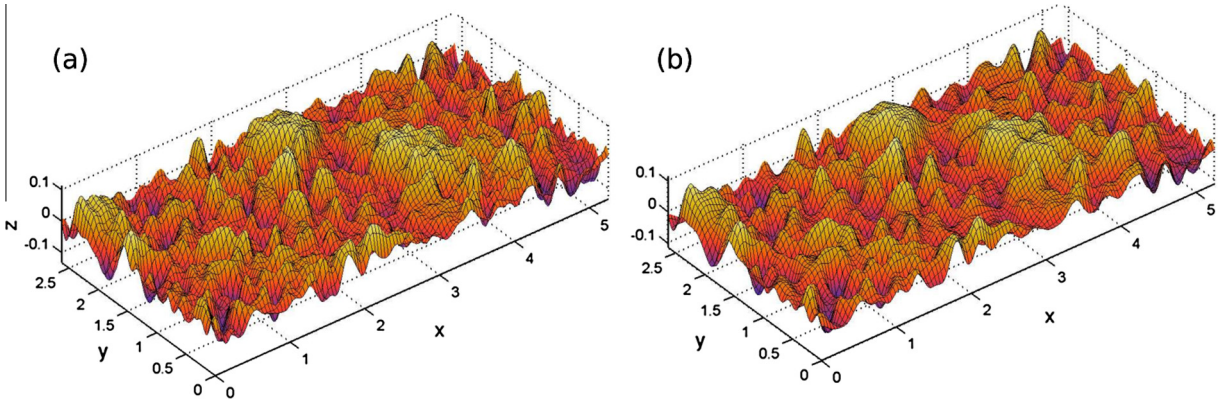

Fig. 4. (a) 3D surface data obtained from a graphite sample. (b) The surface data after the filtering step.

simulations with periodic boundary conditions, a smoothly varying periodic surface is required. If this is not the case unphysical jumps in the surface would occur at the edges of the computational domain, where the periodic boundary conditions are applied. The use of periodic boundary conditions is imposed by computational constraints. If the periodic boundary conditions were not used, a much larger computational domain would be needed to ensure independence from the boundary conditions employed at the inlet and outlet of the domain. Lastly, an accurate representation of the smallest roughness scales would in most cases require an extremely high resolution leading to very large grid sizes and excessive computational requirements.

The problems outlined above can be resolved by filtering the measured surface data in Fourier space using a low-pass filter to obtain an approximate model of the 3D-surface topography. First, the discrete Fourier transform of the surface $\tilde{h}_{\mathrm{raw}}(k_x, k_y)$ is found. Here $k_x = \frac{p}{\Delta s M}$ and $k_y = \frac{q}{\Delta s N}$ are the streamwise and spanwise components of the two-dimensional wavevector, where $p = -\frac{M}{2}, -\frac{M}{2}+1, \ldots, \frac{M}{2}-1$ and $q = -\frac{N}{2}, -\frac{N}{2}+1, \ldots, \frac{N}{2}-1$. The 2D power spectrum of the surface shown in Fig. 4(a) is illustrated in Fig. 5. As expected, the low wavenumber modes dominate the power spectrum and high wavenumber modes make only a very small contribution. In order to remove high-wavenumber contributions a circular low-pass filter

$$f_c(k_x, k_y) = \begin{cases} 1 & \text{for} \quad k_x^2 + k_y^2 \leqslant k_c^2, \\ 0 & \text{for} \quad k_x^2 + k_y^2 > k_c^2, \end{cases} \tag{1}$$

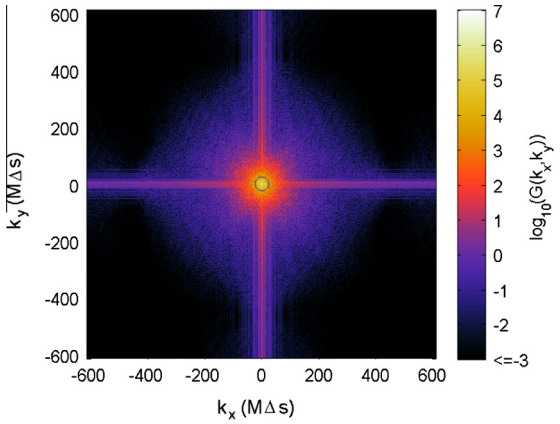

Fig. 5. Area power spectral density of the graphite surface shown in Fig. 4(a). The small grey circle indicates the extent of the low-pass filter used to create the filtered surface shown in Fig. 4(b). The cross pattern visible is due to aliasing effects induced by the jumps present at the periodic boundaries for the unfiltered surfaces.

is applied, which removes all contributions above a certain wavenumber k_c

$$\tilde{h}(k_x, k_y) = \tilde{h}_{\mathrm{raw}}(k_x, k_y) f_c(k_x, k_y). \tag{2}$$

The filtered surface $h(x, y)$ corresponds to the inverse Fourier transform of $\tilde{h}(k_x, k_y)$ and is therefore described by a continuous and

differentiable analytic function. Since the filtered surface consists of a superposition of sine and cosine functions which are periodic over the given domain, the resulting filtered surface varies smoothly across the boundaries. The low-pass filter will also remove most of the measurement noise. The value for the cut-off wavenumber k_c needs to be chosen with care. If it is chosen too low the filtered surface will not resemble the raw surface data sufficiently. A too high value for k_c will result in surface structures on very small scales that are expensive to resolve in direct numerical simulations. The optimal level of filtering depends on the surface topography, and thus no general recommendation can be given. The influence of the level of surface filtering on the fluid dynamical properties will be discussed in depth in the second part of this paper in Section 3.

The Fourier filtering approach taken in this work is not the only way to obtain a continuous periodic surface. Bons [7] and Wu and Christensen [62] mirrored surface data in the streamwise and spanwise direction in order to cover larger areas in wind tunnel experiments. Mirroring has the disadvantage that the resulting surfaces are in general not differentiable at the mirror boundaries, which may not be in keeping with the character of the given surface. Furthermore, mirroring would not be suited to some types of anisotropic rough surfaces, e.g. surfaces with ribs that have a much higher slope on the windward faces compared to the slope on the leeward faces of the ribs.

2.3. Grid dependence

Due to computational constraints it is not possible to conduct a grid refinement study for every surface studied in this paper. Therefore, the grid dependence has been tested for a representative example (shown in Fig. 4(b)), corresponding to the surface 24×12 discussed in Section 3.

The general consensus regarding the grid spacing in the wall-normal direction for the simulation of smooth-wall turbulent channel flow is that a high resolution is required close to the wall $\Delta z^+ < 1$ for $z^+ \lessapprox 10$ and that a lower resolution is sufficient to resolve the flow at the channel centre $\Delta z^+ \approx 5$ (see [23,20,40]). In rough-wall simulations, the smallest grid spacing is employed near the wall, and a higher grid spacing is used near the channel centre as in the smooth wall case. The required near-wall resolution is less well defined, since it is influenced by the roughness geometry and the strength of the roughness effect on the flow, i.e. whether the flow is fully rough or in the transitionally rough regime. Leonardi et al. [33] and Orlandi et al. [45] employed a grid spacing $\Delta z^+ \lessapprox 1$ within the roughness layer, i.e. in the range $\min(h(x,y)) \leqslant z \leqslant \max(h(x,y))$, whereas Coceal et al. [15] showed that a larger wall-normal grid spacing ($\Delta z^+ \gg 1$) is sufficient to resolve the flow around cubic obstacles for a case that was dominated by form drag, i.e. that could be considered as fully rough. Since all of the cases studied here fall into the transitionally rough regime, a uniform grid spacing with $\Delta z^+ < 1$ is used throughout the roughness layer. Above the roughness layer the wall-normal grid spacing is gradually increased, reaching a maximum spacing of $\Delta z^+_{\max} \approx 5$ at the channel centre.

Predicting an adequate grid spacing in the streamwise and spanwise directions is more difficult. Since the roughness is distributed approximately uniformly over the surface, a uniform grid spacing is used in the streamwise and spanwise directions. For smooth wall channel flow a grid spacing of $\Delta x^+ \approx 10$ in the streamwise and $\Delta y^+ \approx 5$ in the spanwise direction is usually employed (see [23,40,39,19,20]). These numbers are given by the need to resolve the near wall-streaks, which are aligned with the streamwise direction (see [23,25]). Rough walls are known to break up the near-wall streaks (provided that the roughness effect is strong enough) leading to a more isotropic form of turbulence near the wall (see [1,54,3,43]). This implies that for rough-wall turbulent flow the streamwise and spanwise grid spacing should be approximately the same; therefore, from the fluid dynamics viewpoint a resolution of $\Delta x^+ \approx \Delta y^+ \approx 5$ seems sensible. However, the required resolution also depends on the topography of the rough surface. If the rough surface possesses features on very small scales an even higher resolution may be required. Since in the present study the rough surfaces are represented by a Fourier series, the size of the smallest features can be estimated by the smallest wavelength present in the Fourier series $\lambda^{\min}$.

In order to investigate the resolution requirements for the finest surface structures a grid refinement study has been conducted where the streamwise and spanwise resolution was varied (see Table 1). A filtered scan of the graphite sample with $k_c = 24/L_x$ was used as a rough surface. In all cases the same wall-normal resolution was used, where $\Delta z^+_{\min} = 0.667$ and $\Delta z^+_{\max} = 4.13$. The simulations were run at a Reynolds number $Re_\tau = 180$. The domain size was $5.25\delta \times 2.625\delta \times 2\delta$. As can be observed from Fig. 6, the results for the mean streamwise velocity profile and the normal Reynolds stresses show a good agreement in the nx576, nx384 and nx288 cases. The variation in the roughness function ΔU^+ (see Table 1), which has been computed by subtracting the centreline velocity from the centreline velocity in the corresponding smooth-wall reference case $\Delta U^+ = U_c^{\text{ref}} - U_c$ (see [9]), is small. Only for the coarsest grids can a significant difference be observed. The nx192 case gives a slightly higher mean streamwise velocity and a higher peak value for mean streamwise velocity fluctuations. The spanwise and wall-normal velocity fluctuations are lower for this case. Even in the coarsest case the observed differences compared to the most highly resolved case are small. We can thus conclude that 12 to 16 grid points per smallest wavelength of the surface give a good resolution of the surface topography. In the following simulations a grid spacing comparable to the case nx384 will be used, which ensures a good resolution of the flow for all surfaces investigated in the context of this paper.

In summary, two criteria for the streamwise and spanwise grid spacing have been derived, one based on the expected size of the flow structures ($\Delta x^+ \approx \Delta y^+ \lessapprox 5$) and one based on the surface topography ($\Delta x \approx \Delta y \lessapprox \lambda^{\min}/12$). Which criterion is the limiting one depends both on the surface topography and the Reynolds number, i.e. the size of the viscous length scale. We expect that this criterion will be applicable to most irregular rough surfaces. In developing the resolution criterion we have assumed that the power spectrum of the surface studied decays sufficiently with increasing wavenumber, which should be the case for most irregular rough surfaces. Surfaces with a high contribution to the power spectrum at higher wavenumbers will generally require a finer grid. This is not the case for the surface studied here, which shows a strong decay of the power spectral density with increasing wavenumber (see Fig. 5).

2.4. Domain-size dependence

In the previous subsection, a domain size of $5.25\delta \times 2.625\delta \times 2\delta$ has been employed. This is significantly larger than the minimal flow unit [22], which would have an approximate size of

Table 1
Simulation parameters and mean flow statistics in the grid refinement study.

Case	N_x	N_y	Δx^+	Δy^+	$\lambda^{\min}/\Delta x$	$\overline{U}$	ΔU^+
nx192	192	96	4.9	4.9	8	11.3	4.7
nx288	288	144	3.28	3.28	12	11.0	5.0
nx384	384	192	2.5	2.5	16	11.0	5.0
nx576	576	288	1.6	1.6	24	10.9	5.1

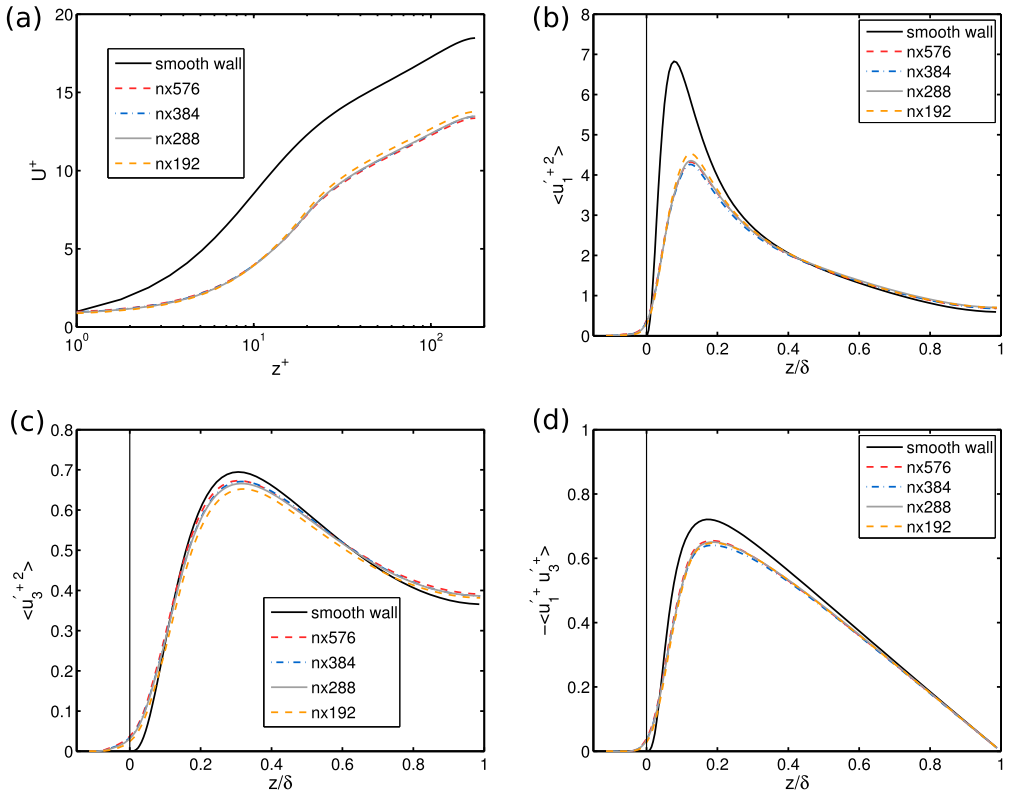

Fig. 6. Grid dependence: mean streamwise velocity profile (a), Reynolds stresses: streamwise (b), wall-normal (c) and shear stress (d).

$1.8\delta \times 0.6\delta \times 2\delta$ at $Re_\tau = 180$. The domain size is however small compared to other simulations of turbulent channel flow where typically domain sizes of $2\pi\delta \times \pi\delta \times 2\delta$ or larger are employed. In principle, it would be possible to extend the domain size in the streamwise and spanwise directions to integer multiples of the present domain size by repeating the surface pattern. Since the resolution of the surface structure requires a dense grid spacing and thus a large number of grid points, using a large domain size in all cases would entail a considerable increase in computational expense.

The influence of the domain size is tested by comparing the flow statistics for a small and a large domain. Since the surface varies periodically in the streamwise and spanwise directions, a larger domain is simply created by replicating the smaller domain size in a 2×2 array. For the larger domain size (size $10.5\delta \times 5.25\delta \times 2\delta$) the same resolution as in case nx384 discussed in the previous subsection has been employed, i.e. a grid of size $768 \times 384 \times 256$ was used. As can be observed from Fig. 7 there is a good agreement for the mean flow profile and the Reynolds stresses between both domains. Similar observations were made in the work of Coceal et al. [15] who studied flow past a cube-roughened wall. They noted that a quite small domain size was sufficient to obtain accurate results for mean flow, Reynolds and dispersive stress statistics in the case of a fully rough flow.

3. Influence of small scale structure on turbulent channel flow

As discussed in Section 2.2, the scanned surface data obtained from the graphite sample had to undergo a filtering step before it could be used as solid boundary for turbulent channel flow simulations. One of the consequences of the filtering is a removal of some of the small-scale surface structures. A very strong level of filtering can lead to a surface which shows little resemblance to the original scan and has significantly different aerodynamic characteristics. However, we expect that the smallest structures of the surface will have little effect on the flow, if a sufficient amount of the surface structure is retained.

3.1. Variation of the surface filtering

The influence of the small-scale structure of the surface is investigated by varying the cut-off wavelength of the low-pass filter. The maximum retained wavenumber was increased in four steps from $k_c L_x = 8$ to $k_c L_x = 32$. In each step, the number of retained Fourier-modes was approximately doubled (see Table 2). The resulting surfaces are illustrated in Fig. 8, while characteristic surface parameters are listed in Table 3, with parameter definitions provided in Appendix B.

The roughness height k of the filtered surfaces, which is based on the mean peak-to-valley height $S_{z,5\times5}$, varies from about 7% to 18% of the channel half-height δ. Thus we can expect that the roughness will modify the entire flow [21]. Cases with high k/δ, as studied here, are of interest in the context turbines operated in harsh environments [6,60], heat-exchangers [21] and tree-canopies [47].

The level of filtering has a strong effect on the surface topography. The most strongly filtered case, 8×4, shows little resemblance to the original surface scan, while the surfaces retaining the highest number of Fourier modes, 32×16 and 24×12, closely resemble the original surface. This trend is also reflected in the characteristic surface parameters shown in Table 3. For the filtered cases the values of the surface height parameters $S_{z,5\times5}$ and $S_{z,\max}$ are always lower than those of the original scan. However, with decreasing level of filtering these parameters approach the reference values. The average and rms surface heights S_a and S_q for the two least filtered cases 24×12 and 32×16 are within 8% of the reference values based on the original scan.

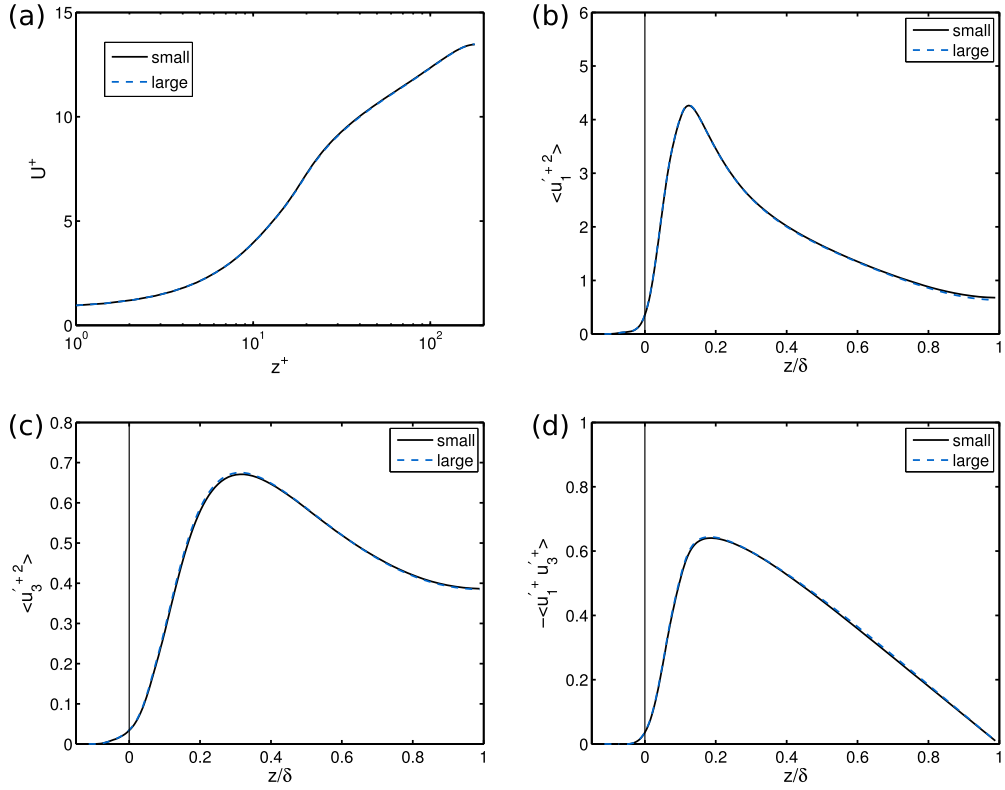

Fig. 7. Domain size dependence: mean streamwise velocity profile (a), Reynolds stresses: streamwise (b), wall-normal (c) and shear stress (d).

Table 2
Simulation parameters, mean velocity and roughness function in filter refinement study. N_{coeff} is the number of retained Fourier coefficients.

Case	8×4	12×6	18×9	24×12	32×16
Δz^+_{max}	4.15	4.61	4.03	4.13	4.55
$k_c L_x$	8	12	18	24	32
N_{coeff}	97	221	503	893	1597
$\overline{U}$	13.5	12.6	11.5	11.0	10.8
ΔU^+	2.5	3.4	4.6	5.0	5.3

The probability density function (pdf) of the roughness height (see Fig. 9) shows that the height distributions obtained for the 32×16 and 24×12 cases show a good resemblance to the height distribution of the unfiltered surface. A similar observation was made by Mejia-Alvarez and Christensen [37] in the context of singular value decomposition for surface filtering. With an increasing level of filtering the differences between the pdf for the filtered cases and the pdf for the original surface become larger; the pdf for the 8×4 case is much narrower than the original pdf. The surface skewness S_{sk} and kurtosis S_{ku} decrease with a decreasing amount of filtering. The least filtered cases have a height distribution that is close to a Gaussian distribution. The correlation lengths of the surface also decrease with decreasing amount of filtering, which is a consequence of the presence of smaller surface structures. In all cases the surface aspect ratio parameter S_{tr} is greater than 0.5, i.e. the surface can be considered as fairly isotropic.

3.2. Influence on mean flow statistics

Simulations of turbulent channel flow were conducted at $Re_\tau = 180$ for each of the five filtered surfaces to assess the influence of the level of surface filtering, i.e. the amount of small-scale structure retained, on the fluid dynamic properties of a surface. Even though the Reynolds number is low compared to the Reynolds numbers in typical applications, we can expect that in the case of rough-wall flow the trends observed at this Reynolds number are representative of the behaviour at higher Reynolds numbers [9].

In all cases, the same streamwise and spanwise grid spacing $\Delta x^+ = \Delta y^+ = 2.46$ was used, complying with the resolution criteria derived in the previous section. The minimum grid spacing in the wall-normal direction was $\Delta z^+_{min} = 0.667$ and the maximum wall-normal grid spacing was $\Delta z^+_{max} < 5$ in all cases. Following the recommendations of Coceal et al. [15] the flow statistics were averaged over at least $400T_k$, where $T_k = k/u_\tau$ is a time scale based on the roughness height k, which is based on $S_{z,5\times5}$ in the current study.

As can be observed from the velocity profiles shown in Fig. 10, there is a clear dependence of the mean streamwise velocity profile on the level of filtering. A high level of filtering (i.e. a surface composed of a small number of Fourier modes), results in a smaller ΔU^+ compared to the least filtered (32×16) case. A strong amount of filtering also leads to an overall reduction of the roughness height of the surface, as can be observed from the parameters given in Table 3. It is thus not surprising that the more strongly filtered surfaces have a smaller effect on the mean profile. The difference between the two cases retaining the highest number of Fourier modes, 24×12 and 32×16 is small, with a difference of approximately 5% in the value of the roughness function ΔU^+. A decrease in ΔU^+ with an increasing amount of filtering was also observed in the wind-tunnel experiments of Mejia-Alvarez and Christensen [37], who obtained low-order representations of an irregular rough surface using singular value decomposition. In the study of Schultz and Flack [49] the authors also found an increase in ΔU^+ after increasing the level of small-scale structure by adding grit to a surface composed of uniform spheres. Based on the convergence of ΔU^+ with an increasing amount of retained Fourier modes we

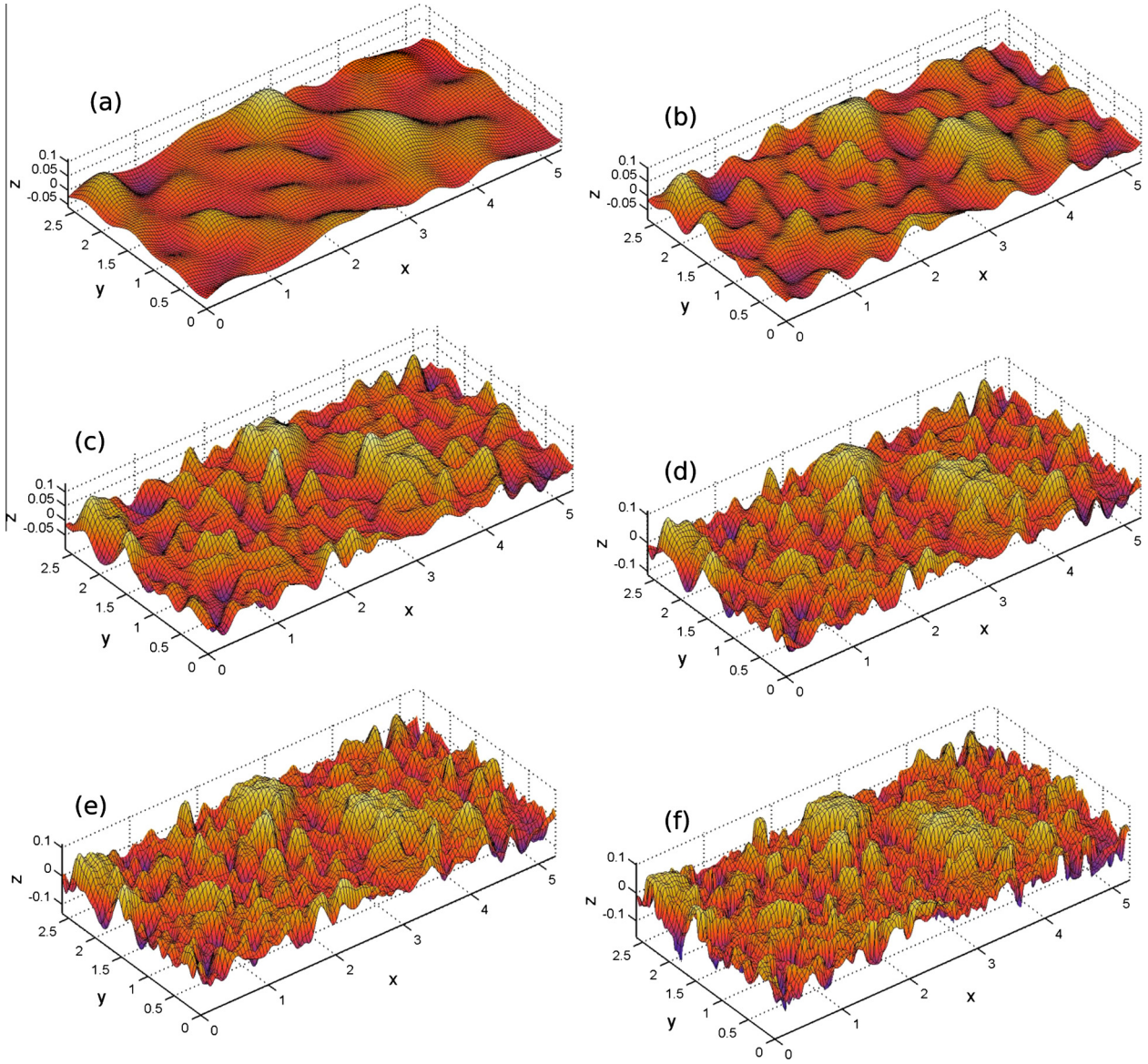

Fig. 8. Influence of different levels of filtering on the surface topography. (a)–(e) filtered cases in order of decreasing level of filtering: (a) 8×4, (b) 12×6, (c) 18×9, (d) 24×12 and (e) 32×16; (f) unfiltered surface.

Table 3
Characteristic parameters (see Appendix B for definitions) for surfaces studied in filter refinement study.

Parameter	8×4	12×16	18×9	24×12	32×16	Unfiltered
S_a	0.0194	0.0236	0.0273	0.0294	0.0305	0.0318
S_q	0.0256	0.0305	0.0349	0.0373	0.0387	0.0402
$S_{z,5\times5}$	0.0739	0.112	0.149	0.167	0.182	0.196
$S_{z,\max}$	0.170	0.186	0.227	0.228	0.246	0.266
S_{sk}	1.15	0.68	0.46	0.28	0.19	0.08
S_{ku}	4.89	3.52	3.24	2.97	2.93	2.87
L_x^{cor}	0.39	0.30	0.24	0.22	0.22	0.21
L_y^{cor}	0.47	0.41	0.43	0.35	0.30	0.27
S_{sl}	0.48	0.41	0.44	0.36	0.30	0.27
S_{al}	0.38	0.29	0.24	0.22	0.22	0.21
S_{tr}	0.80	0.72	0.54	0.61	0.74	0.75

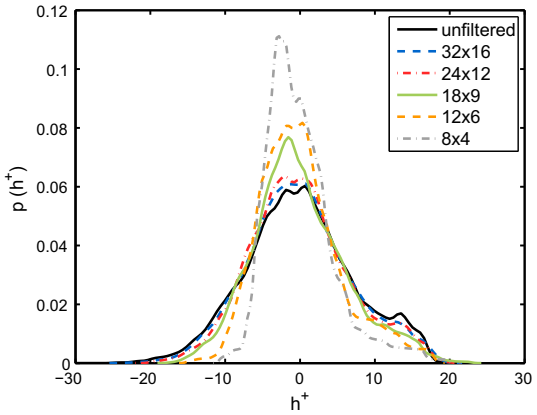

Fig. 9. Probability density function of height values in filter refinement study.

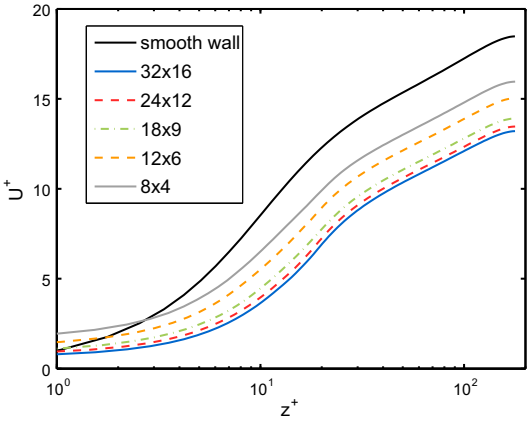

Fig. 10. Mean streamwise velocity profile for different degrees of surface filtering.

can conclude that Fourier filtered versions of a scanned surface give accurate predictions for its roughness effect, i.e. ΔU^+ values, provided a sufficient amount of Fourier modes has been retained.

3.3. Dependence of turbulent fluctuations on the level of filtering

The level of the turbulent velocity fluctuations, here measured by the Reynolds stresses, shown in Fig. 11, is also strongly affected by the level of filtering. This is most prominent for the streamwise velocity fluctuations, since the peak of the streamwise fluctuations is located closer to the wall than the peaks of the spanwise and wall-normal velocity fluctuations [20]. The peak value of the profile decreases with a decreasing level of filtering. This is in agreement with the general observations for rough surfaces, where an increased amount of roughness is accompanied by a reduction of the streamwise velocity fluctuations (see [18,28,27,9]). For the two least filtered cases, 24×12 and 32×16, the Reynolds stresses are in good agreement. In the outer part of the profile, the streamwise Reynolds stress is in good agreement with the smooth-wall reference case. Looking at the spatial distribution of the fluctuations, illustrated in Fig. 12 for a plane normal to the spanwise direction, we can observe that even for the most strongly filtered case the distribution and intensity of the fluctuations shows a marked change compared to the smooth wall reference case. Over most of the near wall region the intensity of the fluctuations is reduced, except in the wake of larger roughness features, where the fluctuations have a similar intensity as in the smooth-wall reference case. With a decreasing amount of surface filtering, the high intensity fluctuations in the wake of larger features tend to become weaker. At the same time, more regions with very low velocity fluctuations are found, since the cavities of the rough wall become deeper. Further away from the wall the distribution of the streamwise velocity fluctuations becomes almost uniform.

The spanwise Reynolds stress shows a far weaker influence of the presence of the roughness. The peak of the spanwise Reynolds stress is slightly increased and there is a higher level of near-wall fluctuations. However, there is no clear dependence on the level of filtering of the rough surface and all rough surfaces give approximately the same results. The far weaker effect of the roughness on the spanwise velocity fluctuations can be attributed to the location of the peak in the smooth-wall reference case. For the Reynolds number under investigation the peak of the spanwise velocity fluctuations is located at $z/\delta \approx 0.2$ whereas the peak of the streamwise fluctuation is closer to the wall at $z/\delta \approx 0.08$. Thus the roughness does not interfere as much with the spanwise velocity fluctuations, since the peak value occurs above the roughness layer in all cases. Significant spatial variations in the spanwise

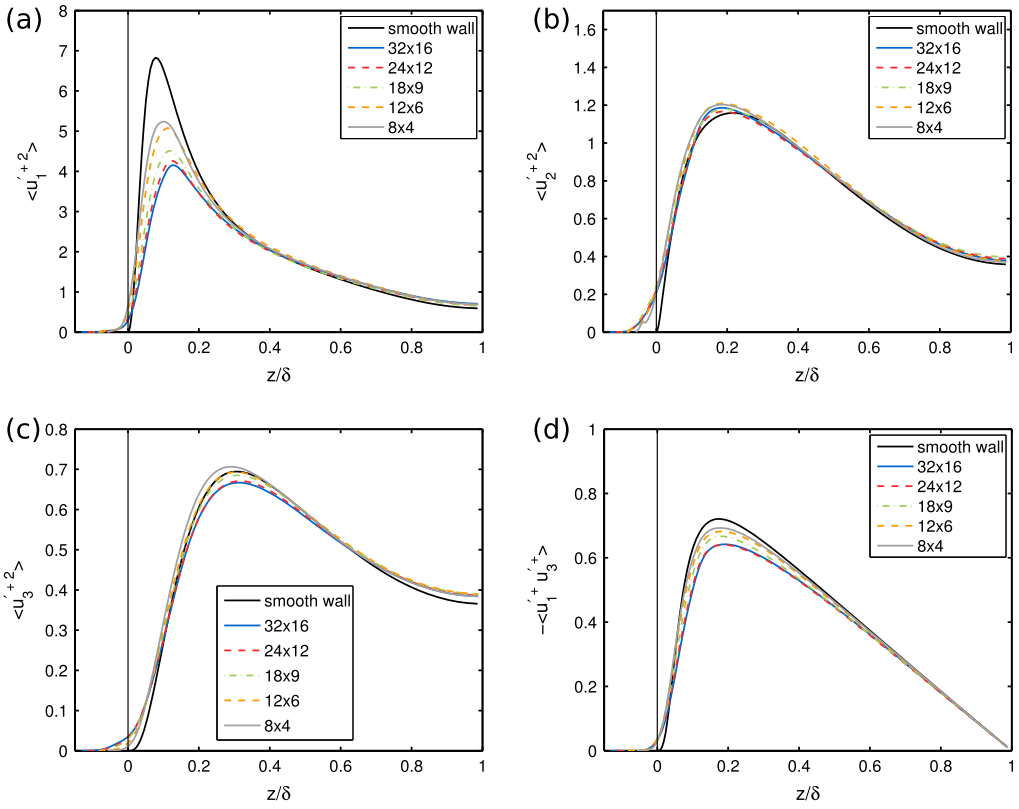

Fig. 11. Influence of surface filtering on velocity fluctuations: (a) streamwise, (b) spanwise and (c) wall-normal components and (d) Reynolds shear stress.

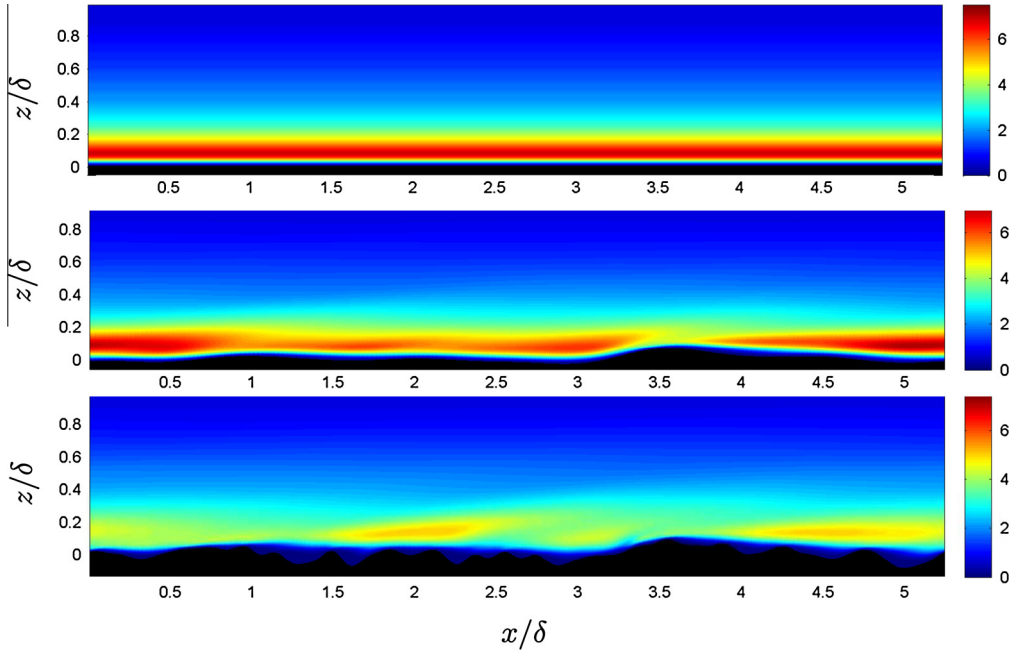

Fig. 12. Time-averaged streamwise velocity fluctuations $\overline{u_1' u_1'}$ in a plane normal to the spanwise direction of the flow. From top: smooth wall, 8×4 and 32×16.

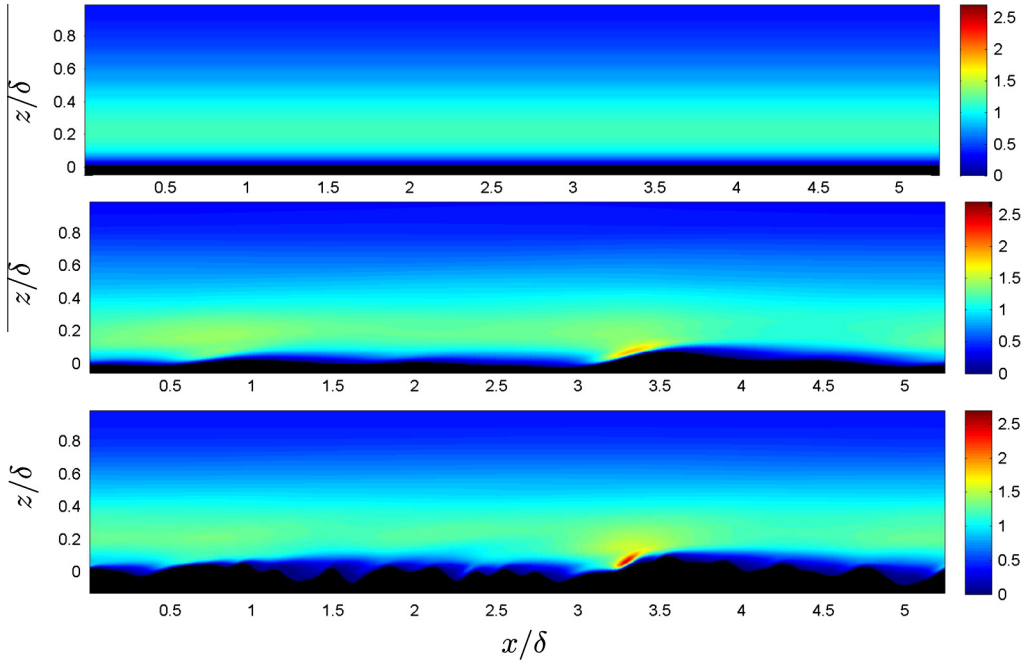

Fig. 13. Time-averaged spanwise velocity fluctuations $\overline{u_2' u_2'}$ in a plane normal to the spanwise direction of the flow. From top: smooth wall, 8×4 and 32×16.

velocity fluctuations mainly emerge at the windward faces of the highest roughness features (see Fig. 13), which may be attributed to time-dependent variations in how the turbulent flow navigates around or over these obstacles. This tendency can be observed for both strongly and weakly filtered surfaces and contributes to a slightly elevated peak value of the profile of the spanwise velocity fluctuations compared to the smooth wall case.

The level of the near-wall wall-normal Reynolds stress is increased for all rough surfaces. This is due to the fact that, in the rough-wall cases, wall-normal velocity fluctuations can occur within the roughness layer, including the mean wall-location. This would not be possible in the smooth wall case. The peak value of the profile is influenced by the degree of surface filtering. For the surface with the highest amount of filtering (8×4) an increase in the peak value of the wall-normal velocity fluctuations is observed which is higher than the peak value in the smooth wall case. For all other cases the peak value is less than or equal to the smooth wall reference case. The peak values decrease with decreasing amount

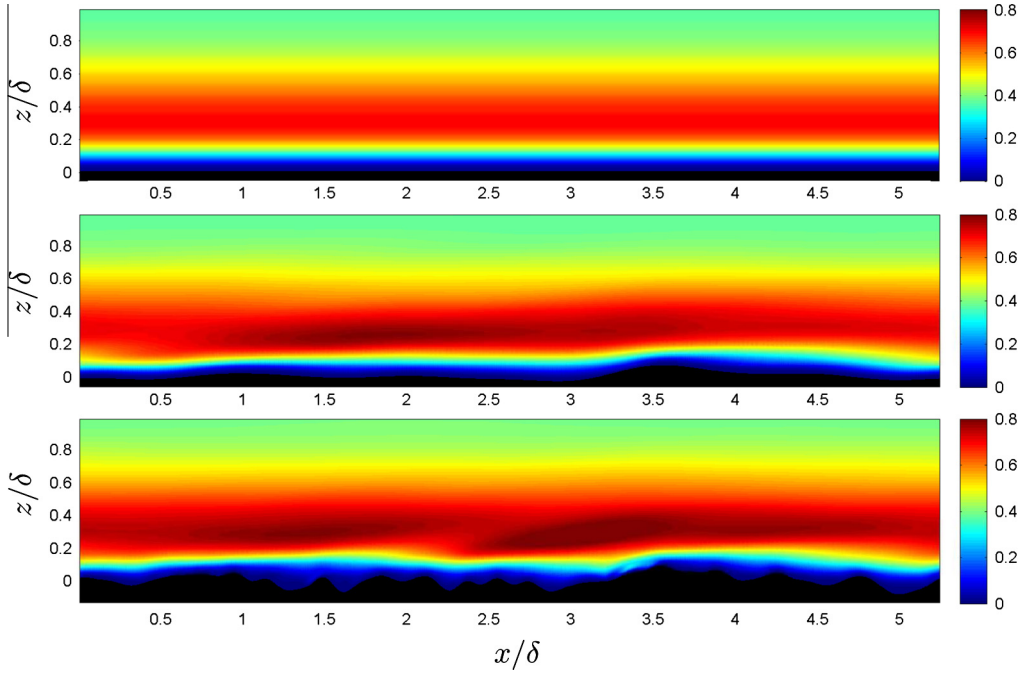

Fig. 14. Time-averaged wall-normal velocity fluctuations $\overline{u_3' u_3'}$ in a plane normal to the spanwise direction of the flow. From top: smooth wall, 8×4 and 32×16.

of surface filtering. The profiles for the two least-filtered cases 32×16 and 24×12 are almost identical.

The spatial distribution of the wall-normal velocity fluctuations are shown on Fig. 14, where it can be seen that regions with higher wall-normal velocity fluctuations tend to form upstream of larger roughness features. These regions are fairly large and occur above the roughness layer at about the location of the peak of the profile. There also exist some very localised regions of high wall-normal velocity fluctuations very close to the wall on the windward slope of the highest roughness features. Their extent is, however, so small that they do not have a significant influence on the mean profile.

Orlandi and Leonardi [44] found that, for surfaces with dense cube or bar-roughness, ΔU^+ increases with increasing wall-normal velocity fluctuations in the crest-plane of the roughness. For the present filtered surfaces an increase of the wall-normal velocity fluctuations with decreasing filtering is only observed in the lower and middle part of the rough wall ($z/\delta \approx 0$). This increase is comparatively small. In the height range of the roughness peaks and above the roughness ($z/\delta \gtrapprox 0.1$) an opposite trend is observed. Here wall-normal velocity fluctuations are strongest for the most strongly filtered case 8×4, which gives the lowest ΔU^+. Some similar observations can be made when looking at the data of DeMarchis et al. [16]: a strong increase of wall-normal fluctuations within the roughness layer can be observed but a decrease (for cases with high roughness) above the roughness layer can be seen.

This shows that observations made for rough surfaces composed of roughness elements like cubes and bars do not necessarily apply to all types of rough surfaces. In the case of dense cube-like roughness very strong fluctuations form in the crest plane of the cubes; for the current roughness no clear crest plane exists and there is a more gradual transition from the flow within the rough surface to the flow above it. The roughness height pdfs of the current rough surfaces are smooth, continuous distributions whereas the pdf of a uniform block roughness would consist of two δ peaks. In addition, the prominent features of the surfaces studied here are far more aerodynamically shaped than block-type roughness. A further factor that may affect the comparison is that the simulations by Orlandi and Leonardi [44] were conducted for a constant mass flow rate, and not for a constant mean streamwise pressure gradient as in the current simulations. A rough-wall and a smooth-wall simulation with the same mean streamwise mass flow rate will result in different values for Re_τ, where Re_τ for the rough wall will be higher. Since the intensity of the wall-normal velocity fluctuations increases with increasing Re_τ (see e.g. [20]), the increase observed by [44] may also partially be attributed to a Reynolds number effect.

DeMarchis et al. [16] investigated flow over irregular rough surfaces which were uniform in the spanwise direction. They also observed a decrease of the peak value of the wall-normal velocity fluctuations. However, this was accompanied by a very strong increase of the near-wall wall-normal velocity fluctuations in the lower part of the rough wall. In the case of the present surfaces such a strong increase is not observed. This can be attributed to the fact that the current surfaces are approximately isotropic, i.e. show a similar variation in structure in the spanwise direction as in the streamwise direction. Hence the flow can detour in the spanwise direction around large surface features, which would not be possible for the surfaces studied by DeMarchis et al. [16]. Thus the level of wall-normal velocity fluctuations induced by the current surfaces is significantly lower.

The Reynolds shear stress behaves like the streamwise velocity fluctuations: it is reduced with a decreasing amount of surface filtering. This is due to an increasing level of dispersive shear stress (see Section 3.4) that arises from flow inhomogeneity in the presence of the roughness. In the outer part of the profile, the Reynolds shear stress shows good agreement with the reference case. The collapse occurs at approximately $z^+ = 100$ which is in agreement with the observations of DeMarchis et al. [16].

In the strongly filtered case 8×4, the area of low shear stress near the wall, where viscous effects dominate, is of approximately uniform thickness and follows the contour of the wall (see Fig. 15). This surface can be considered as wavy. In the cases with more

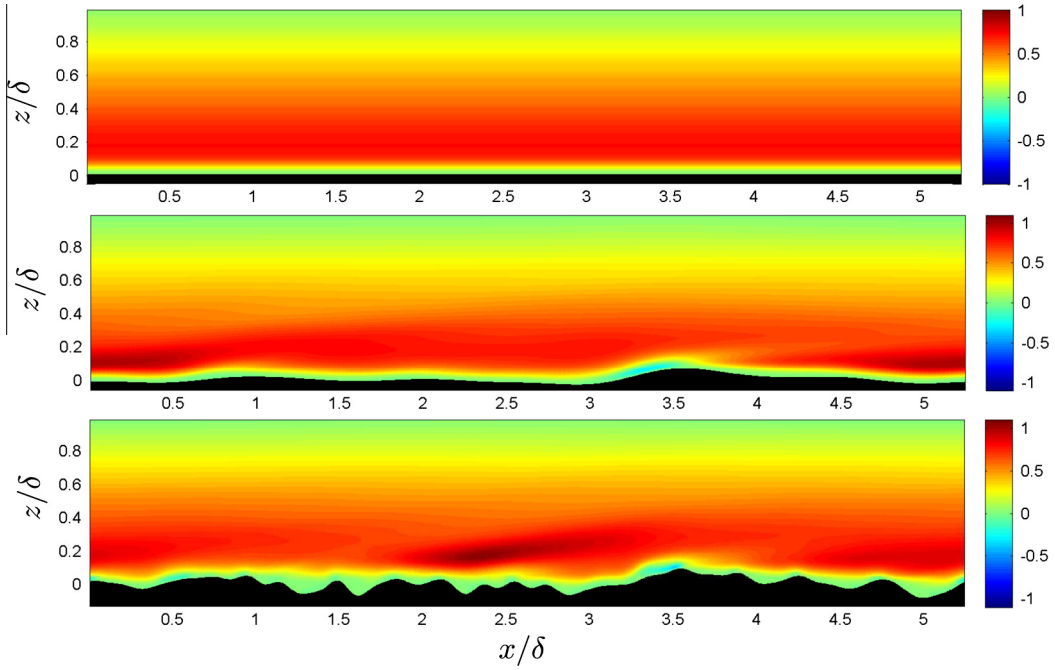

Fig. 15. Time-averaged shear stress $\overline{-u_1' u_3'}$ in a plane normal to the spanwise direction of the flow. From top: smooth wall, 8×4 and 32×16.

small scale structure (24×12 and 32×16), this is not the case. Here the layer of low stress near the wall shows considerable variations in thickness. In all cases, small areas of negative $\overline{-u_1' u_3'}$ can be seen close to the windward faces of higher roughness features. A similar observation was made in the simulations of DeMarchis et al. [16].

3.4. Spatial structure of mean flow field and dispersive stresses

In the rough-wall case the velocity field is not statistically homogeneous in planes parallel to the wall as it would be for a smooth wall channel flow. The velocity components can thus be decomposed as [17,15]

$$u_i = U_i + \tilde{u}_i + u_i'. \tag{3}$$

Here $U_i = \langle \bar{u}_i \rangle$ is the time (over-line) and plane (brackets) averaged velocity for a given horizontal plane, which has been discussed in Section 3.2. $\tilde{u}_i = \bar{u}_i - U_i$ is the spatial variation of the time-averaged velocity, and u_i' represents the turbulent fluctuations, which give rise to the Reynolds stresses discussed in Section 3.3. By analogy to the Reynolds stresses, dispersive stresses can be defined $\langle \tilde{u}_i \tilde{u}_j \rangle$, which describe transfer of momentum by spatial variation in a given horizontal (x-y-) plane. The dispersive stresses are also a measure for the spatial flow inhomogeneity that is induced by the roughness.

The profiles of the dispersive stresses are shown in Fig. 16. A clear dependence of the dispersive stresses on the degree of surface filtering can be observed. Again, convergence of the profiles with decreasing amount of surface filtering is attained. As expected, the magnitude of the dispersive stresses is significantly smaller than the magnitude of the corresponding Reynolds stresses. The exception to this is the streamwise dispersive stress, which is of similar magnitude to the streamwise Reynolds stress in the vicinity of the wall. The dispersive stresses reach their maximum values near the wall and decay towards the centre of the channel. Assuming that the effect of the roughness is confined to the near-wall region, the dispersive stresses should decay to zero far from the wall. Since in all cases currently considered the ratio between channel half-height and roughness height is comparatively small, the values close to the centre of the channel are still finite. These values are of a similar order of magnitude as seen in the study of Coceal et al. [15], who studied flow over large cube roughness, and the values reported in DeMarchis et al. [16] who studied flow over random two-dimensional rough surfaces. In the following, profiles of the dispersive stresses will be discussed in detail in conjunction with the time-averaged flow field.

The profile of the streamwise dispersive stress (see Fig. 16(a)) attains the highest values of all the dispersive stresses shown. A peak can be observed close to the wall within the roughness layer. It is of the same order of magnitude as the peak value for the corresponding Reynolds stress. The highest values are attained for the smoothest of the rough surfaces (8×4), and the streamwise dispersive stress decreases with a decreasing amount of filtering. Thus the streamwise dispersive stress shows an opposite dependence on the surface filtering compared to the streamwise Reynolds stress. The higher peak value for smoother surfaces can be attributed to the fact that for smoother surfaces fewer obstacles exist. Thus areas with large streamwise velocity can emerge within the rough surface (see Fig. 17). At the same time regions with low streamwise velocity exist in the wakes of the highest roughness features for all surfaces considered here. For the surfaces with high wavenumber contributions the formation of areas with high streamwise velocity is impaired by the higher number of roughness features, which leads to an increasing obstruction of the flow. This results in a smaller overall variation of the streamwise velocity at a given distance from the wall.

In the context of the time-averaged streamwise velocity it is also of interest to evaluate the occurrence of reversed flow within the roughness layer. As a measure for reversed flow, the probability of negative time-averaged streamwise velocity $P(\bar{u}_1 < 0)$ has been evaluated as a function of the wall-normal coordinate (see Fig. 18(a)). In the lower part of the roughness there is a high probability (surprisingly close to unity) of negative $\bar{u}_1$ in all cases, indicating that areas of recirculating flow dominate this region. In the

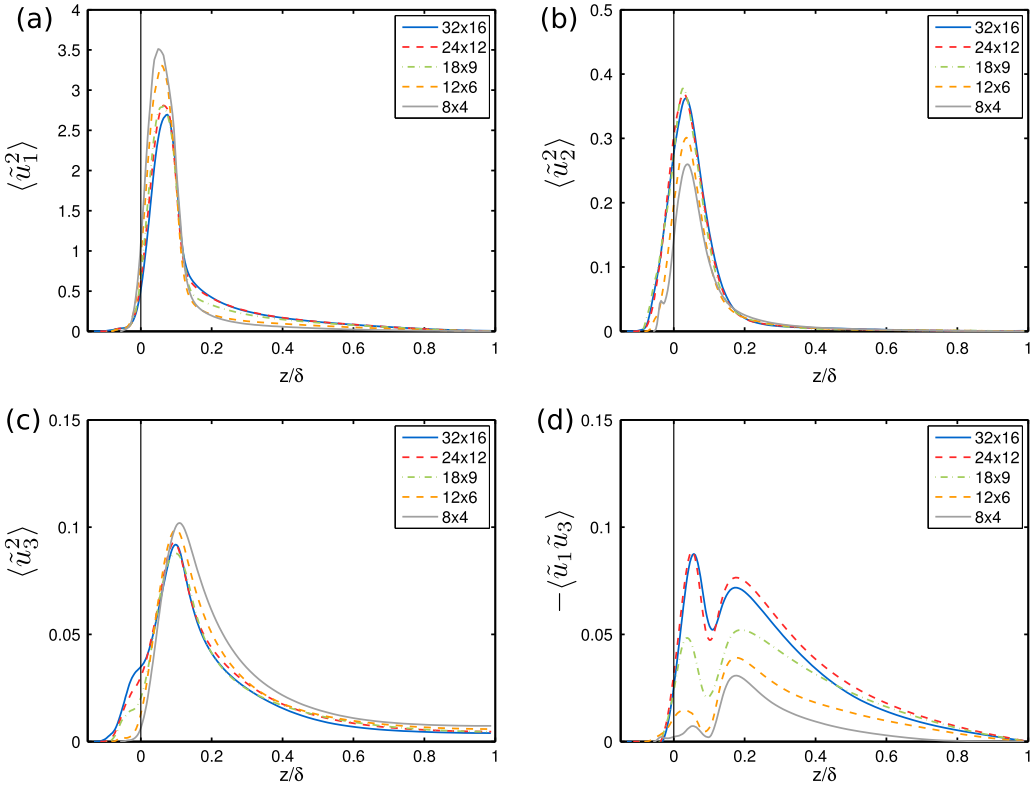

Fig. 16. Influence of surface filtering on dispersive stresses: (a) streamwise, (b) spanwise, (c) wall-normal and (d) shear stress. All velocities shown are normalised with friction velocity.

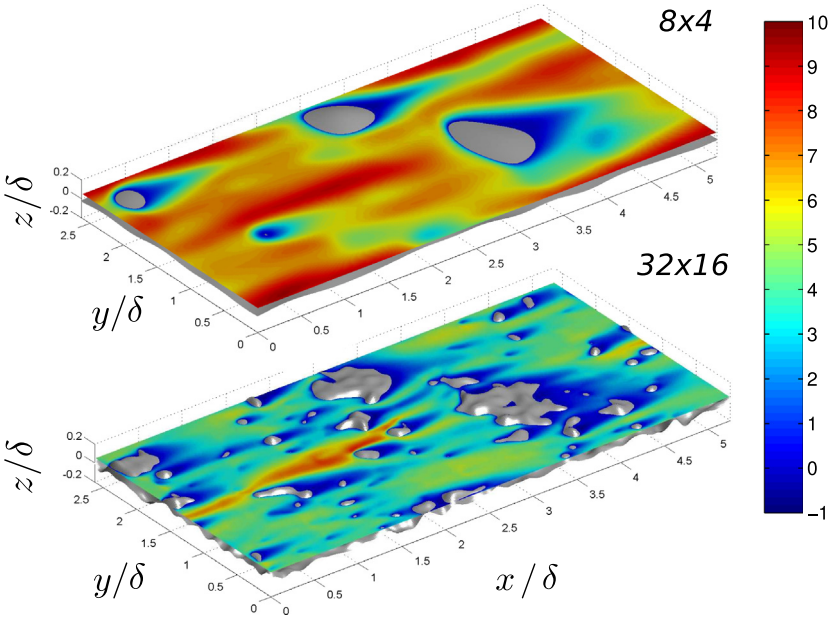

Fig. 17. Time averaged streamwise velocity $\overline{u}_1$ in a plane at $z/\delta = 0.05$ for the surfaces 8×4 and 32×16.

middle and upper parts of the roughness layer there is a clear dependence of $P(\overline{u}_1 < 0)$ on the filtering. With a decreasing amount of filtering the value increases, i.e. there are larger areas of reversed flow for surfaces with features on smaller wavelengths. For the most strongly filtered surfaces reversed flow occurs only in a few areas: in the deepest valleys and behind the largest roughness features (see Fig. 19). For surfaces with contributions at higher wavenumbers the flow is reversed over a far larger area of the surface. Again the flow is reversed in the deeper valleys, which are higher in number. A significant amount of reversed flow up to

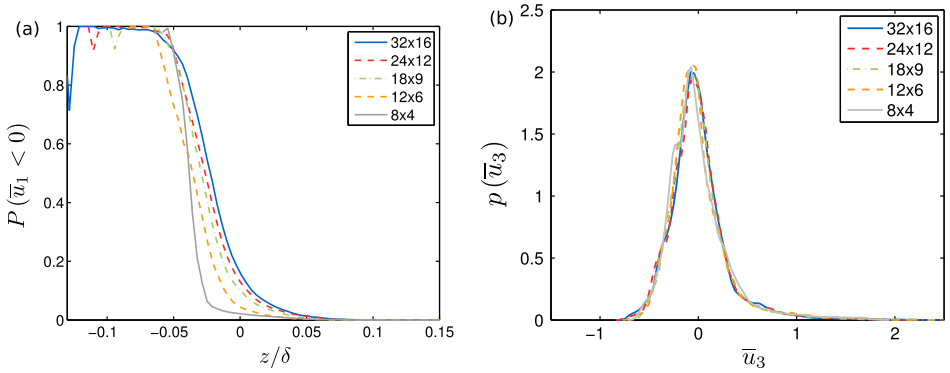

Fig. 18. (a) Probability of negative time-averaged streamwise velocity; (b) Probability density function of time-averaged wall-normal velocity at $z \approx 0.1\delta$.

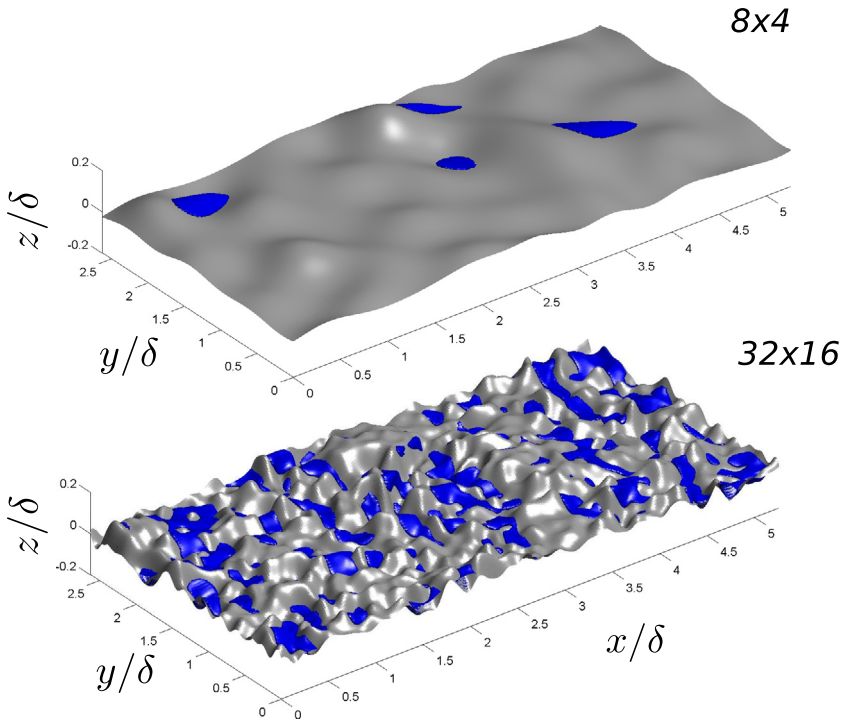

Fig. 19. Isosurfaces of $\overline{u}_1 = -0.01$ (blue) for the surfaces 8×4 and 32×16 (grey). For this plot the z-axis has been stretched by a factor of two to emphasise the relationship between surface structure and areas of reversed flow. (For interpretation of the references to colour in this figure legend, the reader is referred to the web version of this article.)

higher wall-normal locations can be observed where groups of densely spaced roughness features occur (see Fig. 19).

The spanwise dispersive stress (see Fig. 16(b)) is significantly smaller than the spanwise Reynolds stress, but still attains appreciable values in the roughness layer close to the wall. For the spanwise dispersive stress the values tend to increase with decreasing level of filtering, i.e. a higher amount of small scale structure of the surface and an increase in the roughness height. As can be observed from Fig. 20, high values of spanwise velocity occur in the time-averaged flow field mainly near the windward faces of roughness features and between roughness features that are relatively closely spaced in the spanwise direction. For the surfaces with contributions at higher wavenumbers a higher number of more intricately shaped roughness features exists, which promote an increase in spanwise motions of the fluid. However, the smallest features of the surface do not have a strong influence on the mean flow in the spanwise direction; the results for the $18 \times 9, 24 \times 12$ and 32×16 surface are very similar.

The wall-normal dispersive stress is small compared to the wall-normal Reynolds stress (see Fig. 16(c)). It shows a complex dependence on the degree of surface filtering. In the lower part of the roughness layer, the wall-normal dispersive stress increases with decreasing amount of filtering. As discussed above, for the less-filtered surfaces the flow is mostly reversed in the lower part of the roughness layer. In this region strong upward and downward motions of the fluid occur at the windward and leeward faces of some roughness features (see Fig. 21). For the strongly filtered surfaces the wall-normal velocity is close to zero everywhere and shows only weak variations.

In the upper part of the roughness layer, the dependence is reversed, and the smoothest rough surface 8×4 gives rise to the highest wall-normal dispersive stresses. For the most strongly

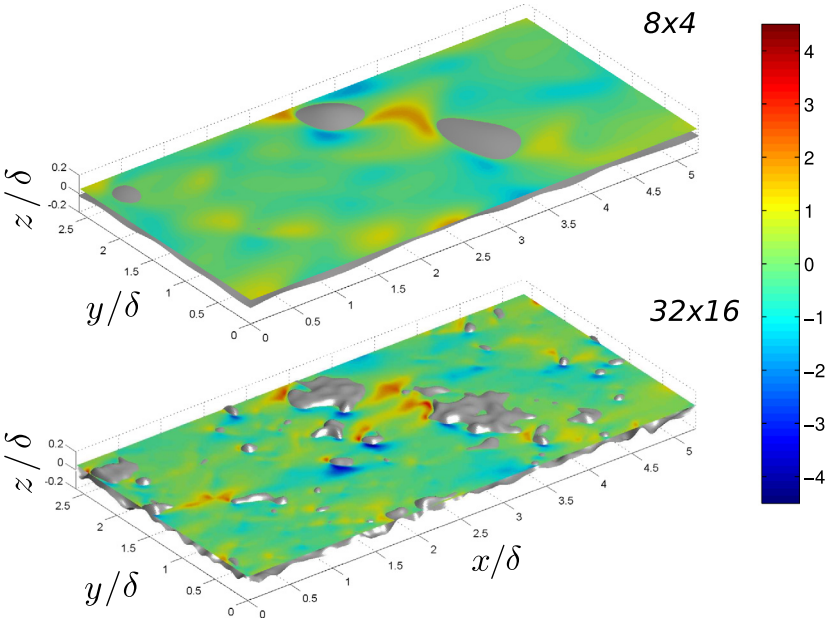

Fig. 20. Time averaged spanwise velocity $\overline{u}_2$ in a plane at $z/\delta = 0.05$ for surfaces 8×4 and 32×16.

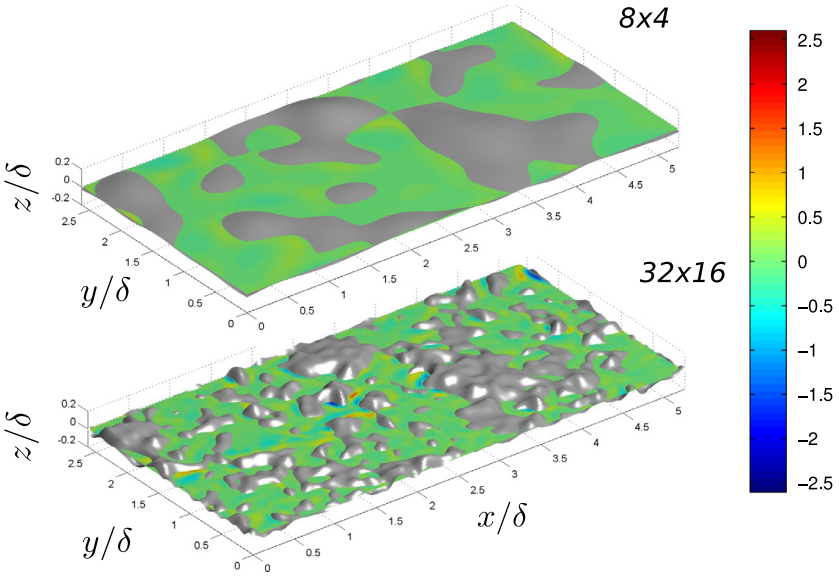

Fig. 21. Time averaged wall-normal velocity $\overline{u}_3$ in a plane at $z/\delta = 0.0$ for surfaces 8×4 and 32×16.

filtered surfaces (8×4 and 12×6) only a few high surface features exist and the near-wall streamwise velocity tends to be higher. The higher roughness features are more exposed and large areas of high wall-normal velocities occur at their windward faces (see Fig. 22). By contrast, the number of higher roughness features increases for the less-filtered surfaces and the peaks are in closer proximity to each other. This leads to an increased shielding, which decreases the extent of strong upward motions at the windward faces of the roughness peaks.

The time-averaged wall-normal velocity tends to attain high positive values at the windward faces of larger roughness features and negative values in their wake. A similar observation was made in the experimental study of Mejia-Alvarez and Christensen [38] on rough-wall turbulent boundary layers. The strength of these upwards and downwards motions can be quantified by looking at the probability density functions of the wall-normal velocity for a given distance from the wall. In the upper part of the roughness layer and close to the rough surface the pdf of the time-averaged wall-normal velocity tends to have a significant positive skewness (see Fig. 18(b)). This indicates that there are weak downward motions of the fluid towards the wall in most areas, accompanied by some localised areas with very high wall-normal velocities where the fluid moves away from the wall.

The dispersive shear stress increases with a decreasing amount of filtering (see Fig. 16(d)). The profile has a complex shape with two peaks, one within the upper part of the roughness layer, and the second further away from the rough wall. For the most strongly filtered case 8×4 the outer peak is considerably higher than the inner peak. This is not the case for the less-filtered surfaces $18 \times 9, 24 \times 12$ and 32×16 where the inner peak is of similar magnitude to the outer peak. The spatial variation of $-\tilde{u}_1\tilde{u}_3$ near the wall shows both areas with high negative and high positive

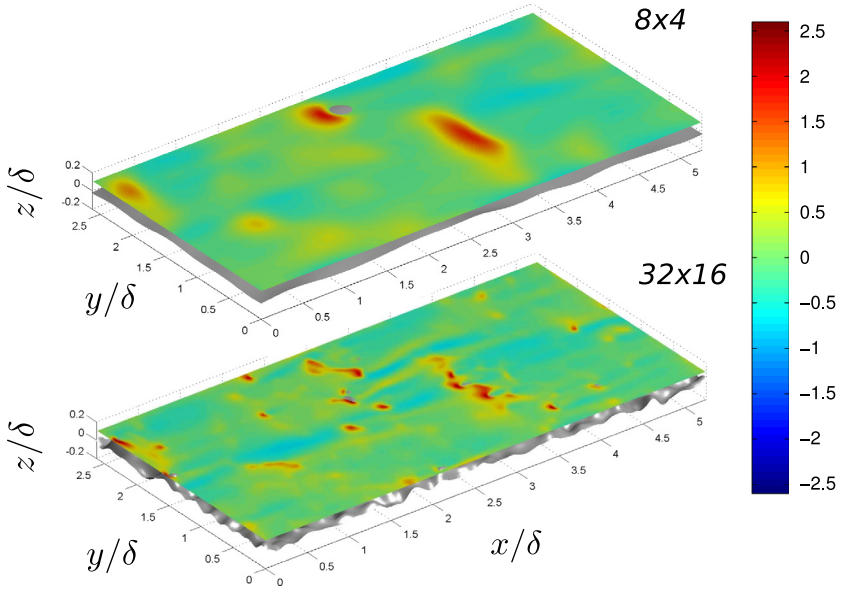

Fig. 22. Time averaged wall-normal velocity $\overline{u}_3$ in a plane at $z/\delta = 0.1$ for surfaces 8×4 and 32×16.

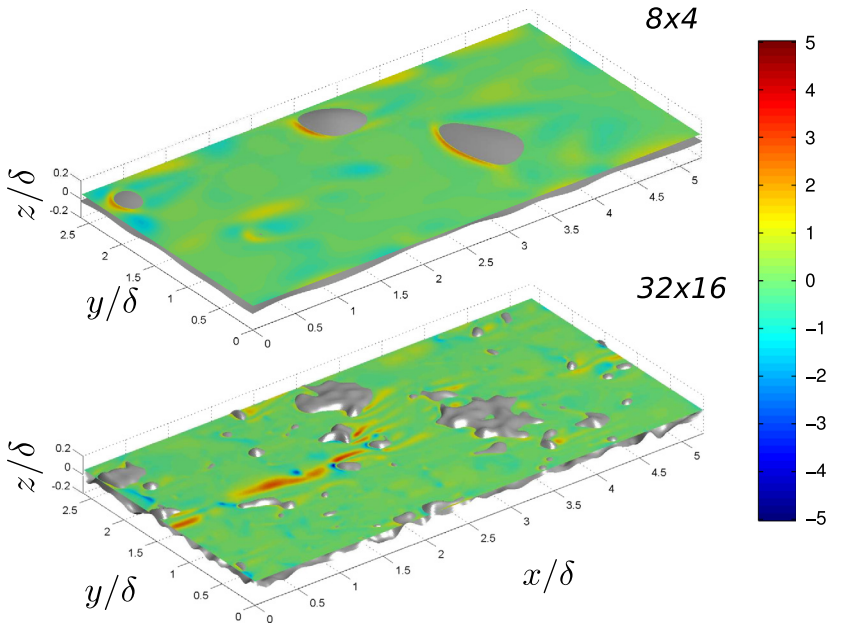

Fig. 23. $-\tilde{u}_1\tilde{u}_3$ in a plane at $z/\delta = 0.05$ for surfaces 8×4 and 32×16.

values. At the location of the inner peak, high positive values occur for more strongly filtered surfaces at the windward slopes of larger roughness features, while negative values tend to occur in the wakes of these features (see Fig. 23). For the surfaces with contributions at higher wavenumbers high positive values appear to be connected to deeper valleys while some spots with high negative values occur above some roughness features of small height. Overall, areas with positive dispersive shear stress dominate over areas with negative dispersive stress giving a small positive average value.

At the location of the outer peak of the profile the spatial variations in $-\tilde{u}_1\tilde{u}_3$ are far weaker (see Fig. 24). Some spots with negative dispersive shear stress occur above the highest roughness features. Again positive dominate over negative values so that a weak positive value emerges for the plane-averaged value for the dispersive shear stress.

The relatively complex structure of the profile for the dispersive shear stress is probably a consequence of the irregularity of the studied rough surfaces, where not all peaks of the surface have the same height. In simulations of turbulent flows past a surface with block-shaped roughness elements of random height Xie et al. [63] found that blocks with random height gave rise to higher dispersive stresses than blocks with uniform height; the random block height also promoted larger variations of the flow within the roughness elements compared to block roughness of uniform height.

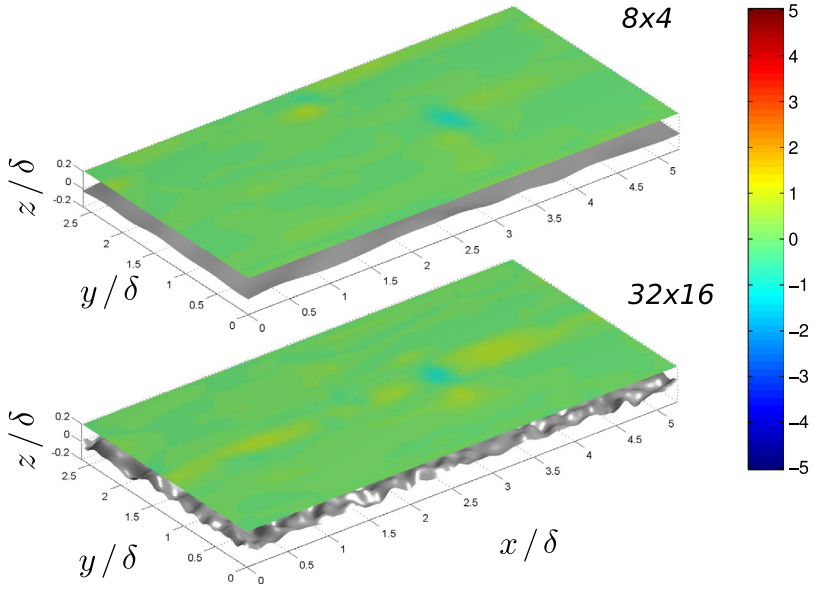

Fig. 24. $-\tilde{u}_1\tilde{u}_3$ in a plane at $z/\delta = 0.2$ for surfaces 8×4 and 32×16.

4. Conclusions

When producing a surface model for an experiment or a numerical simulation on rough-wall flow some form of surface filtering will be unavoidable. The use of a low-pass Fourier filtering has advantages in the context of numerical simulations since it allows the generation of smoothly varying surfaces which obey periodic boundary conditions.

In this work, the use of low-pass Fourier filtering in the context of direct numerical simulations of rough-wall turbulent channel flow was investigated systematically. Small-scale resolution criteria were developed to ensure that both the structure of the surface and the turbulent flow field were resolved adequately. The effects of the low-pass Fourier-filter on the aerodynamic properties were investigated by studying a series of surfaces with a decreasing amount of filtering which were based on a scan of a graphite surface. In general, the flow statistics show a good convergence, once a sufficient amount of small scale structure was retained. However, the mean-flow and turbulence statistics differed significantly if a very low cut-off wavenumber was used.

The simulations also enabled a study of the general effects of small-scale roughness features on turbulent flows, by comparing the results for strongly and weakly filtered versions of the same surface. For the dispersive stresses a complex dependence on the amount of small-scale structure was found. The spanwise and shear dispersive stress showed an increase with an increasing amount of small-scale structure in the surface, whereas the opposite was the case for the streamwise and wall-normal cases. The peak of the wall-normal Reynolds stress decreased with increasing amount of small-scale structure and surface height. In this respect the three-dimensional irregular rough surfaces studied here show a marked difference to previous results on flow past regular cube and bar-roughened surfaces.

Acknowledgements

We would like to thank GasDynamics UK for providing the scanned surface data for the graphite surface. This work has been supported by the Engineering and Physical Sciences Research Council Grants Nos. EP/I032576/1 and EP/G069581/1.

Appendix A. Validation of the embedded boundary method

The data of Maaß and Schumann [35] for turbulent flow in a channel with a lower wavy and a flat upper wall is part of the ERCOFTAC classic database, which is hosted at the University of Manchester (see http://cfd.mace.manchester.ac.uk/ercoftac/).

The lower wall follows a sinusoidal form in the streamwise direction (see Fig. A.25)

$$h(x) = \delta \cos(2\pi x/\lambda), \tag{A.1}$$

with $\delta = 0.05H$ and $\lambda = H$, where H is the mean channel height. The streamwise domain size is $4H$, the spanwise domain size is $2H$. The mean mass flow rate is kept constant and the Reynolds number based on the mean flow velocity and the mean channel height is $Re = H\overline{U}/\nu = 6760$.

A good agreement is found for the mean flow and turbulence statistics (see Fig. A.26). As expected, higher resolution had to be employed compared to the body fitted grid of Maaß and Schumann [35] in order to resolve near wall-structures such as

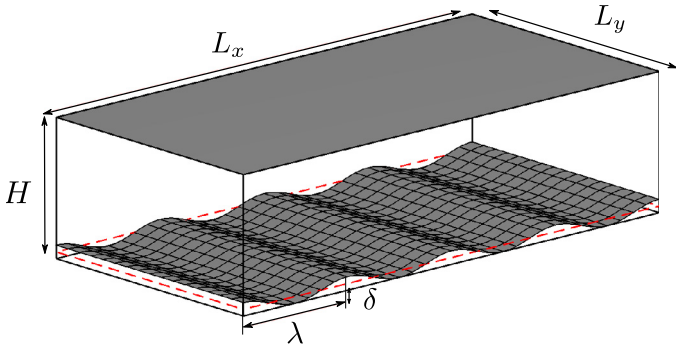

Fig. A.25. Computational domain in ERCOFTAC test case # 77. The lower wall is a sinusoidal surface (amplitude δ, wavelength λ) varying in the streamwise (x) direction. The upper wall is flat.

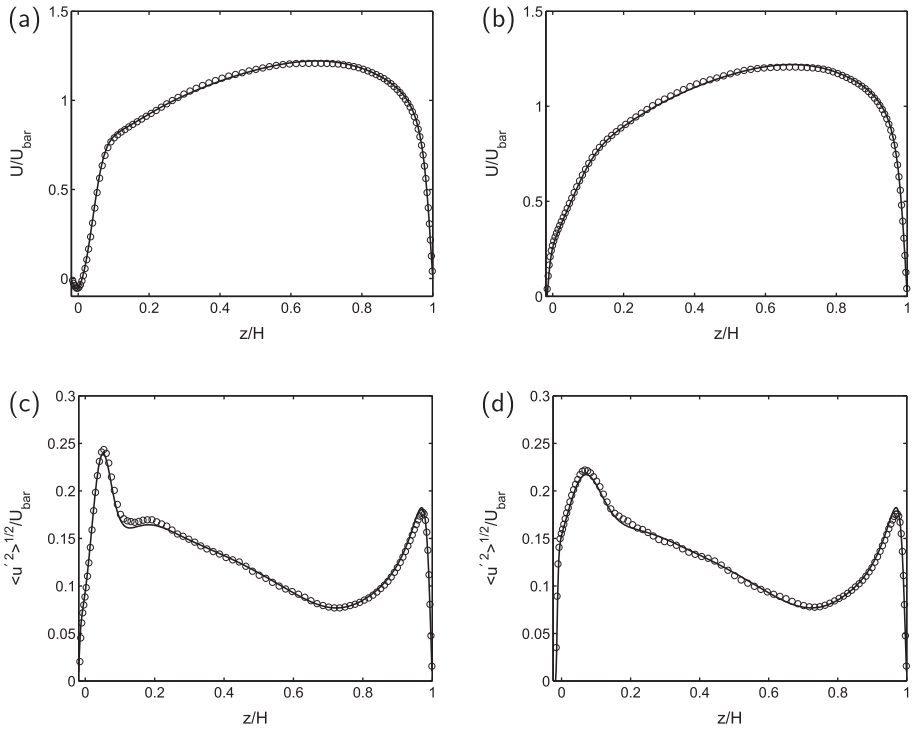

Fig. A.26. Comparison with ERCOFTAC test case # 77. (a), (b): mean streamwise velocity profile; (c), (d): profile of streamwise velocity fluctuations. (a), (c): at $x/\lambda \approx 0.3$ (downwards slope); (b), (d): at $x/\lambda \approx 0.7$ (windwards slope). U_{bar} is the mean streamwise velocity.

Table A.4
Simulation parameters. η denotes the wall-normal coordinate which is curvilinear for the simulation of Maaß and Schumann [35] and equal to z for the iterative embedded boundary case. $u_{\tau,wa}$ is the friction velocity at the wavy wall and $u_{\tau,fl}$ the friction velocity at the flat wall. The viscous length scale has been based on the friction velocity at the wavy wall $u_{\tau,wa}$.

	Δx^+	Δy^+	$\Delta\eta^+_{\min}$	$\Delta\eta^+_{\max}$	$u_{\tau,fl}$	$u_{\tau,wa}$
Maaß & Schumann	10.9	10.9	1.8	13.3	0.070	0.104
Iterative embedded	5.59	11.2	1.2	9.3	0.070	0.106

the thin shear layer which forms on the windward slope of the wavy wall (see Table A.4).

Appendix B. Parameters for the characterisation of rough surfaces

A large range of parameters is used for the characterisation of rough surfaces (see [36]) and the characterisation of rough surfaces is a subject of ongoing research. In the following it is assumed that the mean height of the surface $\overline{h} = \frac{1}{MN}\sum_{i,j}^{M,N} h_{i,j}$, i.e. the mean roughness plane, is zero.

B.1. Amplitude parameters

Amplitude parameters are computed based on the distribution of roughness amplitude. Common measures for the roughness height of a surface are the average roughness height $S_a = \frac{1}{MN}\sum_{i,j}^{M,N}|h_{i,j}|$, the rms roughness height $S_q = \left[\frac{1}{MN}\sum_{i,j}^{M,N} h_{i,j}^2\right]^{1/2}$ and the maximum peak to valley height $S_z = \max(h_{i,j}) - \min(h_{i,j})$. In the context of this study also the mean-peak to valley height $S_{z,5\times5}$ is used. It is found by partitioning a surface into 5×5 tiles of equal size. The mean-peak-to-valley height is then the mean of the difference between the maximum and minimum height of each tile. This measure is a three-dimensional generalisation of the two-dimensional average peak-to-valley height R_z parameter (see [56]).

The shape of a surface can further by characterised by the skewness $S_{sk} = S_q^{-3}\frac{1}{MN}\sum_{i,j}^{M,N} h_{i,j}^3$ and flatness $S_{ku} = S_q^{-4}\frac{1}{MN}\sum_{i,j}^{M,N} h_{i,j}^4$ of the surface height distribution.

B.2. Spacing parameters

Roughness spacing parameters characterise the spacing of the roughness features. They are computed from the areal auto-correlation function

$$R_h(l,m) = S_q^{-2}\langle h_{i+l,j+m} h_{i,j}\rangle. \tag{B.1}$$

The shortest correlation length is defined as

$$S_{al} = \min\left\{\sqrt{(l\Delta s)^2 + (m\Delta s)^2} | R_h(l,m) \leqslant 0.2\right\}. \tag{B.2}$$

The longest correlation length is defined as

$$S_{sl} = \max\left\{\sqrt{(l\Delta s)^2 + (m\Delta s)^2} | R_h(l,m) \geqslant 0.2 \cap (l,m) \in \text{central lobe}\right\}. \tag{B.3}$$

The central lobe of the areal auto-correlation function is the simply connected area where $R_h > 0.2$ that contains the origin $(0,0)$. The ratio of the shortest to the longest correlation lengths gives the surface texture aspect ratio S_{tr}. Surfaces with $S_{tr} \geqslant 0.5$ are in general regarded as close to isotropic, whereas surfaces with $S_{tr} < 0.3$ are strongly anisotropic (see [36]). Similarly, correlation lengths in the streamwise and spanwise direction can be defined $L_x^{cor} = \min\{l\Delta s | R_h(l,0) \leq 0.2\}$ and $L_y^{cor} = \min\{m\Delta s | R_h(0,m) \leqslant 0.2\}$.

References

[1] Antonia RA, Krogstad P-A. Turbulence structure in boundary layers over different types of surface roughness. Fluid Dyn Res 2001;28:139–57.
[2] Arnfield AJ. Two decades of urban climate research: a review of turbulence, exchanges of energy and water, and the urban heat island. Int J Climatol 2003;23(1):1–26.
[3] Ashrafian A, Andersson HI. The structure of turbulence in a rod-roughened channel. Int J Heat Fluid Flow 2006;27:65–79.
[4] Bechert DW, Bruse M, Hage W, VanderHoeven JGT, Hoppe G. Experiments on drag-reducing surfaces and their optimization with an adjustable geometry. J Fluid Mech 1997;338:59–87.
[5] Birch DM, Morrison JF. Similarity of the streamwise velocity component in very-rough-wall channel flow. J Fluid Mech 2011;668:174–201.
[6] Bogard DG, Schmidt DL, Tabbita M. Characterization and laboratory simulation of turbine airfoil surface roughness and associated heat transfer. J Turbomachinery 1998;120:337–42.
[7] Bons JP. St and c_f augmentation for real turbine roughness with elevated free stream turbulence. J Turbomachinery 2002;124:632–44.
[8] Bons JP, Taylor RP, McClain ST, Rivir RB. The many faces of turbine surface roughness. J Turbomachinery 2001;123:739–48.
[9] Busse A, Sandham N. Parametric forcing approach to rough-wall turbulent channel flow. J Fluid Mech 2012;712:169–202.
[10] Cardillo J, Chen Y, Araya G, Newman J, Jansen K, Castillo L. DNS of a turbulent boundary layer with surface roughness. J Fluid Mech 2013;729:603–37.
[11] Castro IP. Rough-wall boundary layers: mean flow universality. J Fluid Mech 2007;585:469–85.
[12] Cheng H, Castro IP. Near wall flow over urban-like roughness. Bound-Lay Meteorol 2002;104(2):229–59.
[13] Claus J, Coceal O, Thomas TG, Branford S, Castro IP. Wind-direction effects on urban-type roughness. Bound-Lay Meteorol 2012;142:265–87.
[14] Coceal O, Belcher SE. Mean winds through an inhomogeneous urban canopy. Bound-Lay Meteorol 2005;115:47–68.
[15] Coceal O, Thomas TG, Castro IP, Belcher SE. Mean flow and turbulence statistics over groups of urban-like cubical obstacles. Bound-Lay Meteorol 2006;121(3):491–519.
[16] DeMarchis M, Napoli E, Armenio V. Turbulence structure over irregular rough surfaces. J Turbulen 2010;11(3):1–32.
[17] Finnigan J. Turbulence in plant canopies. Annu Rev Fluid Mech 2000;32:519–71.
[18] Grass AJ. Structural features of turbulent flows over smooth and rough boundaries. J Fluid Mech 1971;50:233–55.
[19] Hoyas S, Jimenez J. Scaling of the velocity fluctuations in turbulent channels up to retau=2003. Phys Fluids 2006;18:011702.
[20] Hu ZW, Morfey CL, Sandham ND. Wall pressure and shear stress spectra from direct simulations of channel flow. AIAA J 2006;44(7):1541–9.
[21] Jiménez J. Turbulent flow over rough walls. Annu Rev Fluid Mech 2004;36:173–96.
[22] Jimenez J, Moin P. The minimal flow unit in near-wall turbulence. J Fluid Mech 1991;225:213–40.
[23] Kim J, Moin P, Moser R. Turbulence statistics in fully developed channel flow at low Reynolds number. J Fluid Mech 1987;177:133–66.
[24] Kirschner CM, Brennan AB. Bio-inspired antifouling strategies. Annu Rev Mater Res 2012;42:211–29.
[25] Kline SJ, Reynolds WC, Schraub FA, Runstadler PW. The structure of turbulent boundary layers. J Fluid Mech 1967;30:741–73.
[26] Kostof S. The city shaped: urban patterns and meanings through history. London: Thames and Hudson; 1991.
[27] Krogstad P-A, Andersson HI, Bakken OM, Ashrafian A. An experimental and numerical study of channel flow with rough walls. J Fluid Mech 2005;530:327–52.
[28] Krogstad P-A, Antonia RA. Surface roughness effects in turbulent boundary layers. Exp Fluids 1999;27:450–60.
[29] Langelandsvik LI, Kunkel GJ, Smits AJ. Flow in a commercial steel pipe. J Fluid Mech 2008;595:323–39.
[30] Lee JH, Sung HJ, Krogstad P-A. Direct numerical simulation of the turbulent boundary layer over a cube-roughened wall. J Fluid Mech 2011;669:397–431.
[31] Leonardi S, Castro IP. Channel flow over large cube roughness: a direct numerical simulation study. J Fluid Mech 2010;651:519–39.
[32] Leonardi S, Orlandi P, Djenidi L, Antonia RA. Structure of turbulent channel flow with square bars on one wall. Int J Heat Fluid Flow 2004;25:384–92.
[33] Leonardi S, Orlandi P, Smalley RJ, Djenidi L, Antonia RA. Direct numerical simulations of turbulent channel flow with transverse square bars on one wall. J Fluid Mech 2003;491:229–38.
[34] Ligrangi P, Oliveira MM, Blaskovich T. Comparison of heat transfer augmentation techniques. AIAA J 2003;41(3):337–62.
[35] Maaß C, Schumann U. Notes on numerical fluid mechanics, vol. 52. Vieweg; 1996. p. 227–41.
[36] Mainsah E, Greenwood JA, Chetwynd DG, editors. Metrology and properties of engineering surfaces. Kluwer Academic Publishers; 2001.
[37] Mejia-Alvarez R, Christensen KT. Low-order representations of irregular surface roughness and their impact on a turbulent boundary layer. Phys Fluids 2010;22:015106.
[38] Mejia-Alvarez R, Christensen KT. Wall-parallel stereo particle-image velocimetry measurements in the roughness sublayer of turbulent flow overlying highly irregular roughness. Phys Fluids 2013;25:115109.
[39] Min T, Kim J. Effects of hydrophobic surface on skin-friction drag. Phys Fluids 2004;16(7):L55–58.
[40] Moser RD, Kim J, Mansour NN. Direct numerical simulation of turbulent channel flow up to $Re_\tau = 590$. Phys Fluids 1999;11(4):943–5.
[41] Napoli E, Armenio V, De Marchis M. The effect of the slope of irregularly distributed roughness elements on turbulent wallbounded flows. J Fluid Mech 2008;613:385–94.
[42] Nikuradse J. Laws of flow in rough pipes. Tech. rep., NACA Technical Memorandum 1292; 1950.
[43] Orlandi P, Leonardi S. DNS of turbulent channel flows with two- and three-dimensional roughness. J Turbul 2006;7(53).
[44] Orlandi P, Leonardi S. Direct numerical simulation of three-dimensional turbulent rough channels: parameterization and flow physics. J Fluid Mech 2008;606:399–415.
[45] Orlandi P, Leonardi S, Tuzi R, Antonia RA. Direct numerical simulation of turbulent channel flow with wall velocity disturbances. Phys Fluids 2003;15:3587–601.
[46] Pailhas G, Touvet Y, Aupoix B. Effects of Reynolds number and adverse pressure gradient on a turbulent boundary layer developing on a rough surface. J Turbul 2008;9(43):1–24.
[47] Sadeh W, Cermak JE, Kawatani T. Flow over high roughness elements. Bound-Lay Meteorol 1971;1:321–44.
[48] Schlichting H. Experimentelle Untersuchungen zum Rauhigkeitsproblem. Ingenieur-Archiv 1936;7:1–34.
[49] Schultz MP, Flack K. Outer-layer similarity in fully rough turbulent bounday layers. Exp Fluids 2005;38:328–40.
[50] Schultz MP, Flack KA. The rough-wall turbulent boundary layer from the hydraulically smooth to the fully rough regime. J Fluid Mech 2007;580:381–405.
[51] Sherrington I, Howarth GW. Approximate numerical models of 3-d surface topography generated using sparse frequency domain descriptions. Int J Mach Tools Manufact 1998;38:599–606.
[52] Sherrington I, Smith EH. Modern measurement techniques in surface metrology: part I; stylus instruments, electron microscopy and non-optical comparators. Wear 1988;125:271–88.
[53] Sherrington I, Smith EH. Modern measurement techniques in surface metrology: Part II; optical instruments. Wear 1988;125:289–308.
[54] Smalley RJ, Leonardi S, Antonia RA, Djenidi L, Orlandi P. Reynolds stress anisotropy of turbulent rough wall layers. Exp Fluids 2002;33:31–7.
[55] Stout KJ, Davis EJ, Sullivan PJ. Atlas of machined surfaces. Chapman and Hall; 1990.
[56] Thomas TR. Characterization of surface roughness. Precision Eng 1981;3:97–104.
[57] Townsin RL. The ship hull fouling penalty. Biofouling 2003;19:9–15.
[58] van Rij JA, Belnap BJ, Ligrani PM. Analysis and experiments on three-dimensional, irregular surface roughness. J Fluids Eng 2002;124:671.
[59] Wahl M. Marine epibiosis. i. Fouling and antifouling: some basic aspects. Marine Ecol Progress Ser 1989;58:175–89.
[60] Wood RJK, Banaj AS, Turnock SR, Wang L, Evans M. Tribological design constraints of marine renewable energy systems. Philos Trans Roy Soc A 2010;368:4807–27.
[61] Wu Y, Christensen KT. Reynolds-stress enhancement associated with a short fetch of roughness in wall turbulence. AIAA J 2006;44:3098.
[62] Wu Y, Christensen KT. Outer-layer similarity in the presence of a practical rough-wall topography. Phys Fluids 2007;19:985108.
[63] Xie Z-T, Coceal O, Castro IP. Large-eddy simulation of flows over random urban-like obstacles. Bound-Lay Meteorol 2008;129:1–23.
[64] Yang J, Balaras E. An embedded-boundary formulation for large-eddy simulation of turbulent flows interacting with moving boundaries. J Comput Phys 2006;215:12–40.